REVISION 2

**Title:** The (Chemical) Potential for Understanding Overstepped Garnet Nucleation and Growth

**Authors:** Alexandra Nagurney[1], Mark J. Caddick[1], Besim Dragovic[2], Kristen Busse[3]

[1]Department of Geosciences, Virginia Tech, 4044 Derring Hall 926 West Campus Drive, Blacksburg, VA 24061

[2]School of the Earth, Ocean and Environment, University of South Carolina, 701 Sumter Drive, Columbia, SC 29208

[3]ExxonMobil, 22777 Springwoods Village Parkway, Spring, TX, 77289

## Abstract

Overstepping of porphyroblast-forming reactions has been shown to occur in regional, contact, and subduction zone metamorphism, calling into question the paradigm that metamorphic mineral reactions occur at or very close to thermodynamic equilibrium. These overstepped reactions result from the fact that nucleation and growth of new phases requires a thermodynamic driving force, or a *departure* from equilibrium. We use phase equilibria modeling to elucidate the energetic consequences of overstepped garnet nucleation and growth by comparing the chemical potentials of garnet-forming oxide components (MnO, CaO, FeO, MgO, $Al_2O_3$) in two sets of calculations: one in which Gibbs free energy is minimized and one in which the minimization proceeds under identical conditions but in the forced absence of garnet. We focus on twelve examples from the literature which have previously described garnet nucleation as minimally overstepped (garnet nucleation at the *P-T* of initial garnet stability) or garnet nucleation as more substantially overstepped (garnet nucleation at *P-T* conditions greater than initial garnet stability). For a small *P-T* interval above nominal garnet-in reactions, differences in the chemical potentials between the two calculations are commonly minimal. In all

tested examples calculated using two versions of the THERMOCALC thermodynamic dataset, the chemical potential of $Al_2O_3$ ($\mu_{Al2O3}$) diverges between garnet-bearing and garnet-absent calculations at greater *P*-*T* conditions than that of MnO, CaO, FeO and MgO. The *P*-*T* interval between thermodynamic garnet-in and the point at which $\mu_{Al2O3}$ differs substantially between the two sets of calculations appears to be a function of bulk-rock MnO content, reemphasizing the role that small quantities of MnO play in the apparent stability of garnet in calculated phase equilibria. These results highlight the importance of considering multiple thermodynamic datasets, the location of the garnet-in curve, and the abundance of mineral phases in the discussion of overstepped metamorphic reactions. The results have implications for determining kinetic barriers to crystal nucleation and growth, and considering the most appropriate way of defining 'garnet-in' for samples that have experienced overstepping.

**Keywords:** Garnet nucleation, overstepping, thermodynamic modeling, chemical potential, pseudosections

## Introduction

The equilibrium paradigm in metamorphic petrology, in which minerals and fluids continually react with changing pressure (*P*) and temperature (*T*) to achieve the lowest possible Gibbs free energy configuration, has resulted in many significant advances in our understanding of metamorphic and tectonic processes (e.g. Thompson 1957; Essene 1982; Spear and Selverstone 1983; Powell et al. 1998; Kerrick and Connolly 2001; White and Powell 2002; Hacker et al. 2003). Within this paradigm, if the stability of a new phase would decrease the Gibbs free energy (*G*) of the system following a change in *P* and *T* conditions, the departure from equilibrium needed to form that new phase is considered to be negligible and it will nucleate and grow without kinetic barriers. This assumption of equilibrium is consistent with the

metamorphic facies principle (Eskola 1915, 1920), which led to the interpretation of evolving metamorphic conditions using natural mineral compositions and textural information, and facilitated the integration of metamorphic constraints within a tectonic framework. However, recent examples have highlighted rocks in which it appears that deviations from the equilibrium state may have been substantial (>50ºC and >1 kbar), (e.g. Dragovic et al. 2012; Spear et al. 2014; Wolfe and Spear 2018).

Overstepped reactions, typically identified in the metamorphic rock record as cases in which the initial occurrence of a mineral appears to have been at *P-T* conditions significantly greater than its thermodynamically-defined initial stability, have been well-documented (e.g. Ridley and Thompson 1986; Chernoff and Carlson 1997, 1999; Waters and Lovegrove 2002; Zeh and Holness 2003; Wilbur and Ague 2006; Pattison and Tinkham 2009; Pattison et al. 2011; Ague and Carlson 2013; Spear et al. 2014; Carlson et al. 2015a; Castro and Spear 2016; Spear and Wolfe 2018). An alternative observation, of the persistence of phases such as chloritoid, garnet and staurolite beyond the nominal *P-T* limit of their stability, can also be made but is less commonly associated with 'reaction overstepping' (Waters and Lovegrove 2002; Pattison and Tinkham 2009; Pattison & Spear 2018). Broadly, overstepped reactions in the rock record are interpreted to be a consequence of the fact that while pressure, temperature, and bulk composition are the primary controls on metamorphic paragenesis, kinetic impediments to the nucleation of minerals in metamorphic rocks may be substantial and significant (e.g. Ridley and Thompson 1986; Rubie 1998).

The degree of reaction overstepping depends partly on the free energy change of the reaction which, if controlled by temperature, is directly related to its entropy (*S*) (e.g. Fyfe et al. 1958; Ridley and Thompson 1986; Pattison and Tinkham 2009; Pattison et al. 2011). This

suggests that devolatilization reactions with a significant change in entropy ($\Delta S_{rxn}$) should experience 'smaller temperature oversteps' than solid-solid reactions with relatively smaller $\Delta S_{rxn}$ (Ridley and Thompson 1986). However, it appears from comparisons of calculated phase equilibria with natural samples that despite commonly forming from high entropy devolatilization reactions involving breakdown of chlorite, micas, and amphiboles, the nucleation of garnet is frequently overstepped. This has been observed in rocks from contact (e.g. Waters and Lovegrove 2002; Pattison and Tinkham 2009), regional (e.g. Spear et al. 2014; Wolfe and Spear 2017), and subduction (e.g. Dragovic et al. 2012, 2015; Castro and Spear 2016) metamorphic settings and contrasts with other cases in which maintenance of rock-wide thermodynamic equilibrium has been well-demonstrated (e.g. George and Gaidies 2017).

Improved understanding of the conditions and kinetics of garnet nucleation and growth is necessary because garnet is a useful mineral for understanding prograde to peak metamorphic processes. This follows in part from its stability over a wide range of protolith compositions, possible crustal and mantle *P-T* conditions, and from the compositional variations that it and accompanying phases experience during evolving metamorphic conditions, hence its extensive application in quantitative thermobarometry (e.g. Tracy et al. 1976; Ghent 1976; Ferry and Spear 1978; Hodges and Spear 1982; Spear and Selverstone 1983; Spear et al. 1984; St-Onge 1987; Florence and Spear 1991; Konrad-Schmolke et al. 2006; Caddick and Thompson 2008; Moynihan and Pattison 2013). As garnet can also be dated isotopically, this improved understanding can potentially lead to better determination of the rates of tectonic processes (Duchêne et al. 1997; Scherer et al. 2000; Pollington and Baxter 2010; Baxter and Scherer 2013; Dragovic et al. 2015; Baxter et al. 2017; Seman et al. 2017) These examples highlight the

92 importance of making accurate predictions about the likely departures from equilibrium
93 preserved in garnet crystals from a variety of settings.

94 Here, we study metapelitic samples in which previous work has identified that garnet
95 nucleation and growth were overstepped to varying extents, from minimally (i.e. crystals record
96 evidence of growth at approximately the conditions of thermodynamically calculated garnet-in
97 curves for that bulk-rock composition) to more significantly (i.e. initial growth several tens of
98 degrees hotter or several kbars pressure higher than calculated garnet-in). For each sample, we
99 initially calculate the energetic differences between a thermodynamic system in which we
100 minimize free energy and a system that is otherwise identical but in which we prohibit garnet
101 stability. We then examine the differences in the calculated chemical potentials of
102 thermodynamic components (MnO, CaO, FeO, MgO, $Al_2O_3$) between the garnet-present and
103 garnet-absent systems. Our work aims to reveal some of the macro-energetic consequences of
104 overstepped garnet nucleation and growth, while also highlighting possible factors that lead to
105 apparently overstepped metamorphic reactions in pseudosection calculations.

106 **Theoretical Background**

107 **Processes of Crystallization**

108 Several sequential and simultaneous processes are required in order for a metamorphic
109 crystal to nucleate and grow. These can be summarized as: i) breakdown of reactant phases to
110 liberate nutrient components; ii) transport of these nutrients through the intergranular medium,
111 typically in solution within grain boundary fluids but also through solid-state diffusion; iii)
112 homogenous or heterogeneous crystal nucleation; iv) crystal growth via the attachment of atoms
113 or molecules onto the crystal nucleus or surface (e.g. Kretz 1966, 1974; Carmichael 1969; Fisher
114 1978; Walther and Wood 1984; Ridley and Thompson 1986; Rubie 1986; Carlson 1989, 2011).

Each of these processes is inherently complex in natural rocks, but can be understood through the application of appropriate simplifications and rate laws (e.g. Wood and Walther 1983; Walther and Wood 1984; Lasaga 1986; Ridley and Thompson 1986; Lasaga and Rye 1993; Rimstidt 2014). Although these steps most likely coincide in a rock matrix (Carlson 2011), failure of any one of the processes can lead to a (temporary) absence of the product mineral within the rock mass. Sustained failure of one or more of these processes over metamorphic timescales can lead to apparent reaction overstepping, in which an otherwise thermodynamically stable mineral at a given $P$ or $T$ is absent.

Classical views of crystallization in geologic environments include the homogeneous nucleation model, wherein nuclei form via interactions between atoms in solution (Christian 1975). In metamorphic rocks it may be more appropriate to consider heterogeneous nucleation, wherein nuclei develop on pre-existing substrates, thereby lowering interfacial energy (Nielsen 1964; Mullin 1992). Regardless of the nucleation mechanism, a specific molecular cluster size is necessary for a nucleus to mature into an energetically stable crystal. This nucleation step thus exerts a finite requirement on the amount of overstepping for any given reaction (Ridley and Thompson 1986). Few studies have directly quantified the energies required for nucleation in metamorphic rocks (e.g. Rubie et al. 1990; Hacker et al. 1992; Liu and Yund 1993; Rubie 1998; Milke and Heinrich 2002). However, several previous studies have focused on calculating macroscale (rock-wide) energetic differences between rocks containing a particular mineral, typically garnet, and rocks at the same $P$-$T$ but lacking that phase (e.g. Waters and Lovegrove 2002; Pattison and Tinkham 2009; Pattison et al. 2011; Spear et al. 2014; Castro and Spear 2016).

Crystal growth can proceed after this nucleation step, with the rate of growth subject to several criteria. Crystal growth rate can be controlled by element supply, itself a function of reactant mineral breakdown and transport dynamics (i.e. by a diffusion control) or by the energetics of attachment (i.e. by an interface control). Again, each of the processes can be rate-limiting, with a high probability that each one dominated the evolution of some rocks, but played a smaller role in others. Furthermore, one process may be rate-limiting for large parts of the metamorphic history of a rock, but may proceed rapidly during certain phases of crystallization.

For the case of diffusion control, the mobility of the slowest diffusing crystal-building component is likely to control the kinetics and spatial distribution of crystal growth. For example, the local availability of aluminum has been hypothesized as a barrier to garnet crystal growth (e.g. Carmichael 1969; Carlson 2002, 2011; Ketcham and Carlson 2012; Kelly et al. 2013a, 2013b). This is a complex function of the heterogeneous distribution of aluminum in the protolith matrix and the limited solubility of aluminum-bearing species in geologic fluids on grain boundaries (e.g. Manning 2007; Newton and Manning 2007; Carlson 2010, 2011; Carlson et al. 2015b). Such diffusion controlled growth can lead to spatially-ordered porphyroblast distributions (e.g. Hirsch et al. 2000, Carlson 2011; Ketcham & Carlson 2012; Kelly et al. 2013a,b).

In the interface controlled case, the rate of attachment of individual atoms on to the surface of growing crystals controls the net rate of crystal growth (Carlson 2011; Gaidies et al. 2011). The equal availability of nutrients throughout the rock matrix at any given time will result in uniform growth rates and compositional zoning of crystals within a population (Ague and Carlson 2013), with resulting rock textures exhibiting near-random distributions of porphyroblasts (Carlson 2011; Gaidies et al. 2015).

## Application of Equilibrium Thermodynamics to Metamorphic Rocks

Gibbs free energy calculations for metamorphic rocks have helped develop our understanding of the evolution of the Earth's lithosphere. Experimental and empirical constraints on activity-composition (*a*-*X*) models for minerals and fluids have been integrated with datasets of end-member thermodynamic properties (e.g. Berman 1988; Holland and Powell 1998, 2003, 2004, 2011, Powell et al. 1998, 2014; White et al. 2014; Green et al. 2016). Coupled with thermodynamic modeling software, this has resulted in the widespread calculation of pseudosections (or isochemical phase diagrams) to reveal stable mineral assemblages, abundances, and compositions over a range of metamorphic *P*-*T* conditions. Comparisons of calculated phase equilibria with natural samples have resulted in a deeper understanding of the *P*-*T* evolution of metamorphic rocks (e.g. Spear 1993; Tinkham and Ghent 2005; Konrad-Schmolke et al. 2006; Gaidies et al. 2008; Groppo et al. 2009), but have also revealed some challenges to the assumption of whole-rock chemical equilibrium (e.g. Pattison et al. 2011; Guevara and Caddick 2016; Palin et al. 2016; Lanari and Engi 2017; Spear and Wolfe 2018).

Multiple approaches have been proposed for better understanding the development of rocks experiencing deviations from true thermodynamic equilibrium and calculating the compositions of newly-formed phases that will grow after a period of overstepping. This follows from the acknowledgement that the nucleation of new minerals requires departures from thermodynamic equilibrium and energetic driving forces for nucleation (e.g. Rumble 1976; Joesten 1977; Powell 1978). This energetic driving force, or reaction affinity, can be calculated by comparing the energetics of systems containing and prohibiting the stability of a particular phase at a given *P* and *T* (e.g. Pattison et al. 2011; Carlson et al. 2015a). There are three general approaches to calculating the energetics of systems in which the stability of a phase is prohibited.

First, one can assume that all other phases in the rock freely equilibrate to the composition that results in the lowest Gibbs free energy of that system and that the composition of garnet grown following an overstep is the same as the equilibrium composition of garnet at that *P-T* condition if overstepping had not occurred (described as the 'Method 1' calculation of reaction affinity by Pattison et al. (2011)). A second assumption is that the matrix is entirely unreactive in the region of overstepping, so that the compositions of all phases in the rock are fixed in the overstepped interval (Method 2 of Pattison et al. (2011)). A third intermediate approach, often termed the parallel tangent method, is to assume that the compositions of matrix phases can change in the overstepped-region but that the composition of garnet that would grow following overstepping is that which would lower the chemical potential of each thermodynamic component equally (Method 3 of Pattison et al. (2011)).

## Challenges Associated with Applying Equilibrium Thermodynamics to Metamorphic Rocks

Current challenges associated with phase equilibria modelling include: i) making appropriate choices about bulk rock composition and equilibration volume, ii) ascribing appropriate uncertainties to results, and iii) determining the best way to quantify the *P-T* conditions at which minerals nucleate. Careful consideration of 'effective bulk compositions' (Tracy 1982) can help to reduce some of the disparities between calculated rock assemblages and the natural rock record. This is typically implemented by modifying measured rock compositions to remove unreactive phases (e.g. Spear 1988; Marmo et al. 2002; Evans 2004; Konrad-Schmolke et al. 2005; Zuluaga et al. 2005; Caddick et al. 2007; McCarron et al. 2019), by progressively modifying assumed length-scales of chemical equilibrium and calculating 'local compositions' accordingly (e.g. Guevara and Caddick 2016; Lanari and Engi 2017), or by

206 modifying bulk composition so that appropriate mineral compositions are calculated at *P-T*
207 conditions that have been independently constrained (Spear and Wolfe 2018). Each of these
208 calculation methods involves its own set of assumptions about the length scale of equilibrium,
209 reactivity of phases, and transport of material, and will likely result in a different effective bulk
210 composition. Additionally, the choice of equilibration volume and method for determining the
211 bulk composition (the geologic uncertainty) leads to uncertainties in the calculated equilibria
212 (Palin et al. 2016). Finally, there are uncertainties associated with the mineral and fluid end-
213 members and *a-X* models involved in a calculation (Powell and Holland 2008). The propagated
214 uncertainty on the size and position of each calculated mineral assemblage field, and on the
215 abundances and compositions of co-existing phases, depends on the uncertainties on each
216 calculated phase, and is still poorly quantified in most cases.

217 Several methods have been used to determine the *P-T* of garnet nucleation from phase
218 equilibria, with each method having its own benefits and challenges. First, the composition of
219 garnet calculated in a pseudosection at any *P-T* may be assumed to relate directly to the
220 composition of garnet that would exist in a natural rock at that *P-T* condition. Thus isopleths
221 calculated for garnet compositions measured from natural crystal cores (expressed as $X_{alm}$, $X_{sps}$,
222 $X_{grs}$, $X_{pyp}$) are thought to reveal the *P-T* of early garnet growth (e.g. Tinkham and Ghent 2005), in
223 what we hereafter refer to as the 'garnet core isopleth intersection' method. This method has
224 been widely used, but has been questioned for cases in which elastic thermobarometry on
225 inclusions in garnet imply trapping at *P-T* conditions well above those of initial garnet stability
226 in a pseudosection (e.g. Spear et al. 2014; Castro and Spear 2016).

227 Alternatively, the parallel tangent method has been proposed as a more appropriate way
228 to determine the conditions of garnet nucleation following overstepping, by calculating the

garnet composition which would lead to the greatest reduction of Gibbs free energy following a defined interval of overstepping (Thompson and Spaepen 1983; Hillert and Rettenmayr 2003; Hillert 2008; Gaidies et al. 2011; Pattison et al. 2011; Spear et al. 2014). In this case, it is assumed that the chemical potentials of each garnet-forming thermodynamic component would be reduced by the same amount upon garnet nucleation, solving to find the garnet composition at a given *P* and *T* that would achieve this. This method has currently been applied to few samples (rocks from the Sikkim, Himalaya, Sifnos, Greece, the Eastern Vermont terrane, and the Nelson Aureole: Gaidies et al. 2011; Pattison et al. 2011; Spear et al. 2014; Castro and Spear 2016; George and Gaidies 2017; Spear and Wolfe 2018; Wolfe and Spear 2018), and it is unclear how well a methodology that was derived to study homogeneous nucleation in binary metallic melts (Thompson and Spaepen 1983) translates to heterogenous nucleation in metamorphic rocks (see Gaidies et al. 2011 for a discussion on some of the challenges of this method).

With careful consideration of the associated challenges, equilibrium-based thermodynamics can be utilized to study the energetic consequences of overstepped garnet nucleation and growth. Here, we use equilibrium thermodynamics to elucidate the way that the chemical potentials of rock forming components are affected by the failure of garnet to nucleate. We show that chemical potentials of each garnet-forming component behave differently between a garnet-present and garnet-absent phase equilibria calculation. While previous works have used calculated chemical potential gradients to study metamorphic textures (e.g. White et al. 2008; Stipska et al. 2010; Powell et al. 2019), we stress that our phase equilibria calculations do not reveal anything about the atomistic mechanisms of crystal nucleation and growth in natural rocks. Instead, by studying the evolution of chemical potential by the failure of garnet to nucleate and grow, we can explore the role that each component has on the energetics of the system.

## Choice of Samples

We use twelve well-described samples from the literature that have been shown to have experienced various extents of overstepping of garnet-in reactions. Five representative examples are described in detail in the main text. Details of the remaining seven are presented as Supplemental Material, with their results summarized in the main text. For detailed descriptions of the geologic setting for each of these samples, the reader is directed to the original studies describing the samples. The apparent *P-T* of garnet nucleation and previously reported extent of overstepping for each of these samples are summarized in Table 1.

### Examples with Minimal Overstepping (<10ºC and 0.5 kbar)

Sample 24-99 is a sample from the garnet zone of the Lesser Himalaya in Sikkim (Dasgupta et al. 2009; Anczkiewicz et al. 2014; Gaidies et al. 2015; George and Gaidies 2017; George et al. 2018). Previous work suggests that the *P-T* of garnet nucleation (determined by garnet core isopleths) occurred at the garnet-in curve, (Gaidies et al. 2015) and subsequent calculations of the *P-T* of garnet nucleation using the parallel tangent method determined an overstep of <10ºC and 0.4 kbar (George and Gaidies 2017), indicating that the departure from equilibrium during garnet nucleation was negligible.

Sample 35F03 is from the Rappold Complex of the Austroalpine Crystalline Basement of the eastern European Alps (Gaidies et al. 2008). Previous work on this sample suggested that the *P-T* of garnet nucleation (determined by the intersection of garnet core isopleths) occurred at or close to the *P-T* of initial garnet stability, suggesting minimal overstepping (Gaidies et al. 2008).

Additional samples (described in more detail Supplemental Material Part I) that experienced little apparent overstepping are W122, from the Danba Structural Culmination of

eastern Tibet (Weller et al. 2013) and DM_06_128 from the Kootenay Arc of British Columbia (Moynihan and Pattison 2013).

**Examples with Apparent Overstepping (>10ºC and 0.5 kbar)**

Sample TM549a is from the eastern flank of the Strafford Dome in the regional Barrovian sequence of eastern Vermont, and has been cited as providing evidence that overstepping may be important in regional metamorphic terranes (Spear et al. 2014). Thermo-barometric constraints for TM549a indicate that garnet nucleation occurred at 450-500ºC and 4-5 kbar (Menard and Spear 1994). Spear et al. (2014) used quartz-in-garnet barometry to determine the entrapment pressure of quartz inclusions in garnet cores, calculating an isochore extending from 440ºC at 6.7 kbar to 580ºC at 9.0 kbar, contrasting significantly with the earlier thermo-barometric results. While these varying *P-T* estimates lead to different interpretations of the amount of overstepping of the garnet-in reaction, Spear et al. (2014) quantify the overstepping of the garnet nucleation to be 10ºC and 0.6 kbar.

Sample AV26A is from the Pomfret Dome, southeastern Vermont (Bell et al. 2013). It formed during the Appalachian Taconic Orogeny, when over-thrusting of thick tectonic sheets resulted in porphyroblast nucleation at 550ºC and 8.0 kbar, consistent with 30ºC and 1.5 kbar of overstepping (Bell et al. 2013). Analysis of inclusion trail geometries reveals that garnet only nucleated and grew during the start of crenulation-forming deformation events and nucleation was controlled by microlithologic domains developed during deformation (Bell et al. 2013).

Sample 93-CW-4 is from the Nelson Contact Aureole, British Columbia (Pattison and Vogl 2005; Tomkins and Pattison 2007; Pattison and Tinkham 2009; Gaidies et al. 2011; Pattison et al. 2011). Closely-spaced mineral isograds and chemical zoning in garnet suggest that garnet nucleation was delayed until the rocks reached temperatures coincident with the stability

297 of higher-grade porphyroblasts (staurolite and andalusite; Pattison and Tinkham 2009). Garnet
298 nucleation was initially calculated to be overstepped by 30ºC (Pattison and Tinkham 2009).
299 Gaidies et al. (2011) reported overstepping of 6-17ºC, which equates to the maximum driving
300 force for garnet nucleation occurring at 545ºC and 3.5 kbar, the *P-T* conditions of nucleation that
301 we use in this study.

302 Additional samples experiencing apparent overstepping (described in Supplemental
303 Material Part I) are 12TM16 from the Grenvillian Flinton Group of southeastern Ontario
304 (McCarron et al. 2014), ED34 from the Menderes Massif of southwest Turkey (Etzel et al.
305 2019), D13-75 from the Central Himalayan metamorphic core (Iaccarino et al. 2017), TH203B
306 from the Albion Mountains of Idaho (Kelly et al. 2015), and SSFM307-7G from the Funeral
307 Mountains, California (Craddock Affinati et al. 2020).

308 ## Methods

309 ### Calculation of Phase Equilibria

310 Equilibrium mineral assemblages were re-calculated for these samples, using the
311 thermodynamic modeling program Perple_X, version 6.8.3 (Connolly 1990, 2005). Calculations
312 initially used the 'ds5.5' update to the Holland and Powell (1998) internally consistent dataset
313 and the following solution models: biotite (Powell and Holland 1999), chlorite (Holland et al.
314 1998), chloritoid, garnet, staurolite (Holland and Powell 1998), ilmenite (ideal), muscovite
315 (Coggon and Holland 2002), and plagioclase (Fuhrman and Lindsley 1988). ds5.5 was used to
316 maintain consistency with the original literature, with phase equilibria for all but one of the
317 samples that we study here originally calculated with ds5.5. The only exception is Eastern
318 Vermont sample TM549a (Spear et al. 2014), with the original calculations using the modified
319 thermodynamic dataset from Spear and Pyle (2010). We also recalculated five examples using

the updated 'ds6.2' (Holland & Powell 2011) and *a-X* models from (White et al. 2014a), to compare the effects of thermodynamic data on pseudosection topologies and $\Delta\mu_{component}$ calculations. While several comparisons between ds5.5 and revised dataset ds6.2 are now available (White et al. 2014a; Pattison and DeBuhr 2015; Guevara and Caddick 2016; Lanari and Duesterhoeft 2019; Waters 2019; Starr et al. 2020), additional comparison is useful here, as it will shed light on whether the chemical potential trends that we observe above are applicable more broadly, or are artifacts of the specific *a-X* models chosen. The bulk composition and garnet core compositions for all samples are listed in Supplemental Material Part II.

Calculations utilized the chemical system $MnO–Na_2O–CaO–K_2O–FeO–MgO–Al_2O_3–SiO_2±TiO_2$, with $H_2O$ in excess. $TiO_2$ was only included when deemed appropriate by the authors of the original works, in an attempt to maintain consistency. Ferric iron content was not reported in the source papers for any of these samples, so all iron was considered ferrous.

Two pseudosections were calculated for each sample. We first calculated the lowest possible free energy mineral-fluid configuration (i.e. a conventional pseudosection), hereafter termed the true equilibrium calculation or TEC and shown in Figure 1A for a hypothetical sample. This found the identity, abundances and compositions of stable phases as a function of *P* and *T* (see methodology in Connolly and Kerrick 1987; Connolly 1990, 2005). We then recalculated phase equilibria using the same input data, but prohibiting the stability of garnet by excluding its end-members. This calculation, defined here as the Metastable Calculation (MSC) and shown in Figure 1B, involves the assumption that in the forced absence of garnet stability, all other phases will react to reach an alternate lowest Gibbs free energy configuration of the system. As seen in Figure 1B (and in all cases described below), at the *P-T* conditions at which the garnet core isopleths intersect, the only difference in the mineral assemblages between the

TEC and MSC is the lack of garnet in the MSC. At temperatures substantially above garnet-in in the TEC, additional differences in mineral assemblage do occur, but these *P*-*T* regions are not relevant to this study.

**Chemical Potential Calculations**

Chemical potentials ($\mu_{component}$) define the compositional dependence of the Gibbs free energy and are calculated here to understand the energetic consequences of the failure of garnet to nucleate at garnet-in (defined as the curve in *P*-*T* space along which garnet first appears in the TEC). At any *P*-*T* point, a Gibbs free energy versus composition (*G*-*X*) diagram can be used to visualize stable mineral assemblages (Figure 1C; Gibbs 1928; Joesten 1977; Powell 1978; Spear 1993), with the lowest energy tangent line determining the stable phases at that condition (e.g. Phase X and Phase Z in Figure 1C). The chemical potential of each component can then be defined by the intersection of the tangent with the Y-axes (Figure 1C; Gibbs 1928; Joesten 1977; Powell 1978; Spear 1993). This can be extended to three or more dimensions, with the number of stable phases and chemical potentials increasing accordingly (e.g. Figure 1D).

Chemical potentials were extracted from the Perple_X output for the TEC and MSC of each sample. The differences in chemical potentials between the TEC and MSC at a range of *P* and *T* conditions were then calculated, e.g. for MgO:

$$\Delta\mu_{MgO} = \mu_{MgO}^{TEC} - \mu_{MgO}^{MSC} \quad (1)$$

Figure 1E shows variations in $\Delta\mu_{component}$ versus temperature for the theoretical example in Figure 1A-B along a simple 1-D burial and heating path (shown in Figure 1A). As in all examples described below, the *P*-*T* path was determined by defining the shortest possible path between garnet-in in the TEC and the *P*-*T* point at which garnet core isopleths intersect in that diagram. This provides a consistent method for determining the *P*-*T* path for each sample. At *P*-

*T* conditions below initial garnet stability in the TEC (515ºC and 4.1 kbar), both calculations are energetically identical, so $\Delta\mu = 0$ for all components (Figure 1E). At greater *P* and *T*, garnet is stable in the TEC but absent in the MSC, so the two systems have increasingly different energetic configurations. In Figure 1E, $\mu_{MnO}$, $\mu_{CaO}$, and $\mu_{FeO}$ become increasingly negative towards greater *T*, implying that the partial molar free energy of MnO, CaO, and FeO, is lowered by the stability of garnet in the TEC. A positive $\Delta\mu_{component}$, as is the case for MgO in Figure 1E, would imply that the partial free energy of that component is increased by the stability of garnet in the TEC. If $\Delta\mu_{component}$ is zero at any condition greater than initial garnet stability in the TEC, as is the case for $\Delta\mu_{Al2O3}$ up to 550ºC & 4.5 kbar in Figure 1E, then one would infer that the partial free energy of that component in that system is not affected by the stability of garnet. $\Delta\mu_{Na2O}$, $\Delta\mu_{K2O}$, and $\Delta\mu_{TiO2}$ also experience a deviation upon initial garnet stability in the TEC, but are not discussed further here.

Calculated mineral assemblage fields, phase abundances and phase compositions are all subject to propagated uncertainties on thermodynamic data and bulk compositions (Powell & Holland 2008; Palin et al. 2016). However, each of our calculations use the same mineral end-members and thermodynamic data, so some of the absolute errors cancel, and the relative uncertainty between the TEC and MSC for each example is regarded as small (Hodges and McKenna 1987; Powell and Holland 2008; Palin et al. 2016; Hernández-Uribe and Palin 2019). Thus, the uncertainties on chemical potentials calculated from the TEC and MSC for each sample calculated in each dataset would also result in a small relative uncertainty.

**Garnet Composition Calculation**

Our calculations follow Method 1 of Pattison et al. (2011), determining the energetics associated with the failure of garnet to nucleate by comparing two possible equilibrium systems.

The *P-T* conditions of garnet nucleation were constrained by the intersection of isopleths in the TEC calculation, for the purpose of simple comparison with the source papers in which these samples were originally described. Use of the parallel tangent method would instead lead to the calculation of different garnet compositions following overstepping, likely leading to larger apparent oversteps (Pattison et al. 2011; Spear et al. 2014; George and Gaidies 2017). Relevant data for the calculation of the trapping conditions of inclusions in garnet are generally lacking for the samples in this study.

It is important to be able to equate measured garnet crystal core compositions with the composition with which garnet first grew. In three of the samples that we use, garnet core compositions were specifically taken from the centers of the carefully-chosen largest garnet crystals in the rock matrix (Rappold Complex Sample 35E03 from Gaidies et al. (2008); Sikkim Sample 24-99 from Gaidies et al. (2015); Nelson Aureole Sample 93-CW-4 from Gaidies et al. (2011)). In the other examples, we have to assume that the garnet crystals were near-centrally sectioned. We also assume that minimal diffusional modification occurred during or after garnet growth, which is probably appropriate for these samples that reached no greater than low-to-mid amphibolite facies conditions (e.g. Yardley 1978).

## Results

Results for all twelve samples calculated with ds5.5 are summarized in Table 2. Comparisons between the published pseudosections, our recalculations, and the rock samples are described in Supplemental Material Part III and differences are minor. Samples 24-99 (Sikkim, Himalaya), 35F03 (Rappold Complex), AV26A (Pomfret Dome, Vermont), TM549A (Eastern Vermont), and 93-CW-4 (Nelson Aureole) are described in detail below, with samples W122 (Eastern Tibet), DM_06_128 (Kootenay Arc), 12TM16 (Southeastern Ontario), ED34

(Southwest Turkey), D13-75 (Central Himalaya), TH203B (Albion Mountains), and SSFM307-7G (Funeral Mountains), described in Supplemental Material Part IV (Supplemental Figures 1-7).

Results for the five samples calculated with ds6.2 are summarized in Table 3. Comparisons of pseudosections calculated with ds5.5 and ds6.2 are highlighted below for three examples: Sikkim, Pomfret Dome, and Nelson Aureole. Two additional examples (Rappold Complex and Eastern Vermont) and a discussion of the broad differences between ds5.5 and ds6.2 calculations are provided in Supplemental Material Part V and Supplemental Material Figures 8 & 9.

**Behavior of Chemical Potentials in Examples with Minimal Overstepping**

**Sikkim, Himalaya: Sample 24-99:** In the ds5.5 calculation, isopleths calculated for the preserved core compositions of garnet intersect in the TEC at 526ºC and 5.0 kbar, which is coincident with the *P-T* of garnet-in (Figure 2A). Differences in the chemical potentials calculated between the TEC and MSC emerge at garnet-in, producing negative $\Delta\mu_{MnO}$, $\Delta\mu_{FeO}$, and $\Delta\mu_{Al2O3}$ and positive $\Delta\mu_{MgO}$ (Figure 2C). $\Delta\mu_{CaO}$ becomes negative 4ºC after garnet-in, essentially coincident with the *P-T* conditions at which the garnet core isopleths intersect (Figure 2C).

Using ds6.2, garnet core isopleths intersect at 525ºC and 5.2 kbar, which is consistent with essentially no overstepping (3ºC and 0.3 kbar; Figure 2D). At all *P-T* conditions greater than garnet-in in the TEC, $\Delta\mu_{MnO}$ is negative and $\Delta\mu_{MgO}$ is positive (Figure 2F). $\Delta\mu_{Al2O3}$, $\Delta\mu_{FeO}$, and $\Delta\mu_{CaO}$ are initially zero, becoming negative after a short interval, at the *P-T* point essentially consistent with garnet core isopleth intersections (Figure 2F).

The topologies of the pseudosections calculated with each thermodynamic dataset are broadly similar (compare Figure 2A-B with Figure 2D-E), with the main difference being that biotite is stable in ds5.5 calculations at temperatures greater than ~550ºC (Figure 2A), but is stable over the entire *P*-*T* range of the ds6.2 pseudosection (Figure 2D). However, in both the ds5.5 and ds6.2 calculations, biotite is present at the peak *T* conditions of the sample 565ºC (Figure 2, peak *T* from Gaidies et al. 2015). Thus, both the ds5.5 and ds6.2 calculations yield appropriate assemblages at peak metamorphic conditions.

$\Delta\mu_{MnO}$ is negative and $\Delta\mu_{MgO}$ is positive at *P*-*T* conditions greater than initial garnet stability in calculations using both datasets (Figure 2C, 2F). $\Delta\mu_{Al2O3}$, $\Delta\mu_{CaO}$, and $\Delta\mu_{FeO}$ are negative in calculations using both datasets. In ds5.5, $\Delta\mu_{Al2O3}$ and $\Delta\mu_{FeO}$ are negative directly above garnet-in, with $\Delta\mu_{CaO}$ becoming negative 4ºC above garnet-in. The pattern is similar in the ds6.2 calculation, though displaced to a slightly higher temperature. In both datasets, $\Delta\mu$ of all components diverges from zero at a *P*-*T* approximately coincident with the garnet core isopleth intersection.

**Rappold Complex: Sample 35F03:** Along the inferred *P*-*T* path in the ds5.5 calculation, garnet-in is at 531ºC and 4.4 kbar (Figure 3A). Garnet core isopleths do not intersect as tightly in this sample, though spessartine and grossular contents intersect at 531ºC and 4.4 kbar, suggesting little to no overstepping. Again, at *P*-*T* conditions directly above garnet-in, $\Delta\mu_{CaO}$ and $\Delta\mu_{MgO}$ become positive and $\Delta\mu_{MnO}$, $\Delta\mu_{FeO}$, and $\Delta\mu_{Al2O3}$ become increasingly negative (Figure 3C). There is no *P*-*T* interval above garnet-in at which $\Delta\mu$ of any examined component remains at zero.

**Behavior of Chemical Potentials in Examples with Apparent Overstepping**

**Eastern Vermont: Sample TM549A:** The intersection of garnet core isopleths is at 540ºC and 5.8 kbar, suggesting a minimum 35ºC and 1.5 kbar overstep (Figure 4A). Within this apparent overstepped region, $\Delta\mu_{MnO}$ and $\Delta\mu_{CaO}$ become negative and $\Delta\mu_{MgO}$ becomes positive directly after garnet-in (Figure 4C). $\Delta\mu_{FeO} = 0$ for the first 6ºC above garnet-in, before becoming negative. $\Delta\mu_{Al2O3}$ is initially zero, becoming negative at 541ºC and 5.8 kbar, essentially coincident with the *P-T* at which the garnet core isopleths intersect.

Pressure has also been estimated in this sample by quartz-in-garnet elastic barometry. Results from Spear et al. (2014) suggest that, if we assume a temperature of 540ºC, garnet nucleation occurred at 8.0 kbar (their Figure 8). We calculated the $\Delta\mu_{component}$ values along a vector that connects garnet-in in our pseudosection to this *P-T* estimate (Figure 4A,D). At all *P-T* conditions above garnet-in along this vector $\Delta\mu_{MnO}$ and $\Delta\mu_{CaO}$ are negative and $\Delta\mu_{MgO}$ is positive. $\Delta\mu_{FeO}$ becomes negative at 499ºC and 5.1 kbar, and $\Delta\mu_{Al2O3}$ is the final component to experience a deviation between the TEC and MSC at 521ºC and 6.5 kbar (Figure 4D).

**Pomfret Dome, Vermont: Sample AV26A:** In the ds5.5 calculation, Garnet core isopleths for this sample intersect at 540ºC and 7.4 kbar, 38ºC and 2.3 kbar above the closest segment of the garnet-in curve (Figure 5A). Along a simple *P-T* path between these points, a) $\Delta\mu_{MnO}$ is negative at all *P-T* conditions above garnet-in (Figure 5C), b) $\Delta\mu_{CaO}$ and $\Delta\mu_{MgO}$ are both initially zero, deviating at 504ºC and 5.2 kbar, c) $\Delta\mu_{FeO}$ is initially zero, becoming negative at 514ºC and 5.8 kbar, and d) $\Delta\mu_{Al2O3}$ is zero until 530ºC and 6.7 kbar, then becoming negative (Figure 5C). All chemical potentials experience a deviation between the TEC and MSC prior to the *P-T* conditions where the garnet core isopleths intersect.

Using ds6.2, garnet core isopleths intersect at 548ºC and 7.8 kbar (Figure 5D), equating to an approximately 38ºC and 2.3 kbar overstep (Figure 5D). $\Delta\mu_{MnO}$ and $\Delta\mu_{CaO}$ are negative and

$\Delta\mu_{MgO}$ is positive at all conditions greater than garnet-in (Figure 5F). $\Delta\mu_{FeO}$ becomes negative after 518ºC and 6.0 kbar and $\Delta\mu_{Al2O3}$ becomes negative at 520ºC and 6.1 kbar.

The topologies of the ds5.5 and ds6.2 pseudosections are again very similar, containing biotite, chlorite, garnet, muscovite, plagioclase, and quartz in the field where the garnet core isopleths intersect. These intersections also occur at very similar conditions in both calculations and yield identical apparent oversteps in each case. With both datasets, $\Delta\mu$ of all components deviates from zero at or before the *P-T* point at which garnet core isopleths intersect, and in both ds5.5 and ds6.2 $\Delta\mu_{Al2O3}$ is the final component to experience a difference between the TEC and MSC.

**Nelson Aureole, British Columbia: Sample 93-CW-4:** In this ds5.5 example, the calculated garnet core isopleths do not intersect (Figure 6A). We thus assume garnet nucleation at 545ºC and 3.5 kbar, as previously calculated by Gaidies et al. (2011) (their Figure 6B). This coincides with the equilibrium staurolite-in reaction (Figure 6A), so the stability of staurolite was also suppressed in the MSC calculation (Figure 6B). Chemical potential differences generally run parallel to garnet-in reactions unless additional phases such as andalusite are calculated in the TEC (Figure 6C-G). Our choice of an isobaric heating *P-T* path for this contact metamorphic setting is thus unlikely to have a significant effect on the trends in the $\Delta\mu$ calculations. At *P-T* conditions greater than garnet-in in the TEC, $\Delta\mu$ of all components other than MnO is zero for at least an additional 10˚C. $\Delta\mu_{Al2O3}$ diverges last, becoming negative at 528˚C (Figure 6H).

Isopleths for measured garnet core compositions do not intersect in the ds6.2 calculations, where the composition of garnet also never reaches the measured manganese contents of crystal cores ($X_{sps}$ = 0.31), hence the $X_{sps}$ isopleth is not shown in Figure 7A. We thus assume, as in the ds5.5 calculation for this sample, that the *P-T* conditions of garnet nucleation are 545ºC and 3.5

kbar. Along a heating path, $\Delta\mu_{MgO}$ immediately becomes positive at *P-T* conditions greater than garnet-in, while $\Delta\mu_{MnO}$ becomes negative (Figure 7C), $\Delta\mu_{CaO}$ is negative above 448ºC, $\Delta\mu_{FeO}$ is negative above 525ºC, and $\Delta\mu_{Al2O3}$ becomes negative after 539ºC, at slightly lower *T* conditions than assumed garnet nucleation in this sample.

Several significant differences exist between the ds5.5 and ds6.2 pseudosections for this sample (Figures 6 & 7). The stability fields of both garnet and zoisite are expanded in ds6.2 relative to the ds5.5 calculations, which is consistent with other studies (White et al. 2014a; Waters 2019). No substantial differences are apparent in the stability of other phases, including staurolite, with an initial stability at ~545ºC and 3.5 kbar in both cases. As a result of this expanded garnet stability field, there is a greater $\Delta T$ of overstepping in the ds6.2 calculation.

The chemical potential trends are similar in ds5.5 and ds6.2 calculations. In both cases, $\Delta\mu_{MnO}$ immediately becomes negative at the *P-T* of initial garnet stability (Figure 6H, 7C), $\Delta\mu_{Al2O3}$ is the final component to experience a difference, and the *P-T* at which that occurs is nearly coincident with the *P-T* point at which Gaidies et al. (2011) calculated garnet nucleation. There is, however, a greater temperature interval where $\Delta\mu_{Al2O3} = 0$ in the ds6.2 calculation, resulting from the expanded garnet stability field in ds6.2.

## Discussion

### Interpretation of Chemical Potential Calculations

Our calculations show that the chemical potentials of all garnet-forming components typically experience a difference between the TEC and MSC prior to the *P-T* conditions at which garnet nucleates, as inferred from garnet core isopleth intersections.

For samples 24-99 (Sikkim), 35F03 (Rappold Complex), W122 (Eastern Tibet) and DM_06_128 (Kootenay Arc), the garnet core isopleths intersect at effectively the *P-T* of garnet-

in. This can be interpreted as lack of garnet overstepping, agreeing with previous interpretations of these samples (Gaidies et al. 2008, 2015; George and Gaidies 2017). In these examples, $\Delta\mu_{all\ components} \neq 0$ at conditions immediately up-temperature and pressure of garnet-in in the TEC (Figures 2, 3, Supplemental Figures 1-2,8).

In contrast, calculations using both tested datasets for samples 93-CW-4 (Nelson Aureole), AV26A (Pomfret Dome), and TM549a (Eastern Vermont), and calculations using ds5.5 for samples 12TM16 (Southeastern Ontario), ED34 (Southwest Turkey), D13-75 (Central Himalaya), TH203B (Albion Mountains), and SSFM307-7G (Funeral Mountains) show that $\Delta\mu$ of at least one component is zero immediately up temperature of garnet-in. This is represented schematically in Figure 8, in which a hypothetical simplified three-component system is drawn with tangent planes that represent the lowest free energy of the TEC (gray) and the MSC (yellow). In this case, *P-T* conditions exist above garnet-in at which $\mu_{Al2O3}$ is identical in the TEC and MSC, despite differences in $\mu_{MgO}$ and $\mu_{FeO}$ (Figure 8B-C). In the eight overstepped examples shown in this paper $\Delta\mu_{Al2O3}$ is the final component to experience a deviation between the TEC and MSC (Tables 2 & 3).

For certain components (MgO in all examples and CaO for samples 35F03 and 12TM16), $\Delta\mu_{component}$ is positive at *P-T* conditions greater than the TEC's garnet-in. Geometrically, this is shown in Figure 8, in which the tangent planes evolve so that the TEC tangent plane (gray) has a greater $\mu_{MgO}$ than the MSC tangent plane (yellow), resulting in a positive $\Delta\mu_{MgO}$ (Figure 8B-C). This is related to the preferential partitioning of MgO into other phases such as chlorite and biotite at lower to middle amphibolite-facies temperatures (e.g. Ferry and Spear 1978; Holland et al. 1998; Vidal 1999; Lanari et al. 2014). We stress here that while chemical potential gradients drive diffusion in natural systems, the positive $\Delta\mu$ values in our calculations should not be

548 interpreted as diffusional gradients driving MgO and CaO away from a garnet nucleus, with
549 these calculations having no spatial context.

550 **The Key Role of $Al_2O_3$**

551 In the eight examples where overstepping appears to have been significant (Eastern
552 Vermont, Pomfret Dome, Nelson Aureole, Southeastern Ontario, Southwest Turkey, Central
553 Himalaya, Albion Mountains, and Funeral Mountains), $\Delta\mu_{Al2O3}$ persists at or very close to zero
554 until substantially greater *P*-*T* than the TEC's garnet-in (Table 2). This reflects the evolution of
555 TEC and MSC tangent planes (Figure 8B-C). For three out of the eight overstepped examples
556 (Eastern Vermont, Central Himalaya, and Funeral Mountains), the *P*-*T* location at which $\Delta\mu_{Al2O3}$
557 first diverges from zero is at the *P*-*T* at which the garnet core isopleths intersect. In the Pomfret
558 Dome example, $\Delta\mu_{Al2O3}$ becomes negative 10ºC below the *P*-*T* of the garnet core isopleth
559 intersection. In the four remaining examples (Southeastern Ontario, Southwest Turkey, Nelson
560 Aureole, and Albion Mountains), $\Delta\mu_{Al2O3}$ diverges >10ºC below the point at which the garnet
561 core isopleths intersect.

562 It is unlikely that $\Delta\mu_{Al2O3}$ consistently being the final component to diverge between the
563 TEC and MSC results from the choice of *P*-*T* path. In the 2D graph of $\Delta\mu_{Al2O3}$ (Figure 6G), most
564 possible heating paths would lead to a similar result for $\Delta\mu_{Al2O3}$. In the Eastern Vermont
565 example, where we described the evolution of $\Delta\mu$ along two different *P*-*T* paths (Figure 4C,D),
566 $\Delta\mu_{Al2O3}$ is the final component to experience a deviation between the TEC and MSC in both
567 cases. The coincidence of $\Delta\mu_{Al2O3} \neq 0$ and the *P*-*T* of garnet nucleation is more robust for the
568 garnet core isopleth intersection (Figure 4C) than the quartz-in-garnet barometry determination
569 (Figure 4D), indicating that this relationship is partially dependent on the method of determining
570 the *P*-*T* of garnet nucleation.

This is the peer-reviewed, final accepted version for American Mineralogist, published by the Mineralogical Society of America.
The published version is subject to change. Cite as Authors (Year) Title. American Mineralogist, in press.
DOI: https://doi.org/10.2138/am-2021-7354. http://www.minsocam.org/

In all five examples using ds6.2, $\Delta\mu_{Al2O3}$ is the final component to experience a difference between the TEC and MSC (Table 3). In the Sikkim, Rappold Complex, and Nelson Aureole samples, this deviation in $\Delta\mu_{Al2O3}$ occurs within 10ºC of the *P-T* at which the garnet core isopleths intersect. Once again, this suggests that the calculated equilibrium garnet composition at the *P-T* at which $\Delta\mu_{\text{all components}}$ diverge from zero coincides with the preserved compositions of appropriate natural garnet crystal cores.

**The Role of $X_{MnO}$ in Pseudosection Calculations**

The only difference between examples calculated within any given dataset is the bulk-rock composition (compositions are listed in Supplemental Material Part II). In general, samples with lower bulk rock MnO content display the least apparent overstepping of garnet nucleation.

Figure 9 shows TEC and MSC versions of a $T$-$X_{MnO}$ diagram for sample AV26A (Bell et al. 2013) in which the *x* axis ranges from 0 to 0.2 wt.% MnO, with other components fixed in the ratio reported by Bell et al. (2013). The temperature at which garnet stability is first calculated scales inversely with the bulk rock MnO content. At 0.05 wt.% MnO there is a <10ºC difference between garnet-in and $\Delta\mu_{Al2O3} \neq 0$, at 0.10 wt.% MnO, the temperature difference between garnet-in and $\Delta\mu_{Al2O3} \neq 0$ is 35ºC, and at 0.15 wt.% MnO the temperature difference between garnet-in and $\Delta\mu_{Al2O3} \neq 0$ is >75ºC (Figure 9C). Thus, as the bulk-rock MnO content increases, the temperature of garnet-in decreases, and a substantial window opens between garnet-in and the initial decrease of $\Delta\mu_{Al2O3}$. Thus, if $\Delta\mu_{Al2O3} \neq 0$ can be used as an approximate indicator of *P-T* conditions at which garnet nucleation is likely, then rocks with a greater bulk rock MnO might be expected to exhibit more pronounced apparent overstepping of garnet-in reactions. This results from high MnO contents lowering the calculated temperature of garnet-in reactions without significantly changing the equilibrium garnet composition at higher temperatures

(Symmes and Ferry 1992; Mahar et al. 1997; Tinkham et al. 2001; Caddick and Thompson 2008; White et al. 2014b).

Due to the challenges of experimentally creating Mn end-member phases, thermodynamic data for Mn end-members were either calculated based on natural partitioning data in well-equilibrated natural rock samples or estimated based on experimental constraints for other end-members (Mahar et al. 1997) and estimated Margules parameters (White et al. 2014b). Therefore, the uncertainties on the equilibria for Mn-bearing phases are likely greater than the uncertainties on end members with more robust experimental constraints. The strong dependence of garnet-in on the MnO bulk rock content may partially be a function of poorly constrained thermodynamic data or may be impacted by the sequestration of MnO by accessory phases (McCarron et al. 2019). Simply recalculating phase equilibria in a MnO-free system is not an appropriate way to mitigate this phenomenon, with the calculated initial stability of garnet then moving to higher *P-T* than suggested by independent constraints (e.g. White et al. 2014b).

It is also clear that immediately up-pressure and -temperature of calculated garnet-in reactions, calculated volume abundances of garnet in the TEC are extremely small (labeled in panel A of Figures 2-7). In the examples from Sikkim (ds5.5 & ds6.2) and the Rappold Complex (ds6.2), garnet core isopleths intersect at a point at which 0.5% of the calculated rock volume is garnet in the TEC. None of the other calculations suggest core isopleth intersections at conditions at which the TEC predicts the stability of much more than 1% garnet. This suggests that while the *P-T* range of garnet stability appears large, very low abundances of garnet would be expected over much of this range. Even if garnet is stable in a natural rock, abundances of less than 0.5% may not be readily detected in thin section. It is thus important to carefully interrogate the calculated abundances of phases while interpreting pseudosection results.

## Implications

Examples used in this paper are consistent with previous observations that suggest that overstepping of garnet-in reactions occurs in a variety of metamorphic settings (e.g. Pattison and Tinkham 2009; Gaidies et al. 2011; Pattison et al. 2011; Dragovic et al. 2012; Spear et al. 2014; Carlson et al. 2015; Castro and Spear 2016; Wolfe and Spear 2017; Spear and Wolfe 2018). It is thus important to consider: i) the tectonic implications of overstepping, ii) the utility of these chemical potential calculations, iii) the definition of the garnet-in curve, and iv) interrogation of the thermodynamic data.

Comparison of the amount of overstep and geochronological constraints on the duration of garnet growth provide important evidence that overstepping can influence interpretations of tectonic processes. In an example from Sifnos, Greece, garnet experienced a large overstepping of ~100ºC and 7 kbar during subduction, then grew cm-sized crystals in <<1.0 Myr (Dragovic et al. 2012). Other samples in Sifnos experienced an apparently smaller overstep and grew 3–5 cm crystals over ~8 Myr (Dragovic et al. 2015). In the regionally metamorphosed Eastern Vermont terrane (geographically near the samples described by Bell et al. (2013) and Spear et al. (2014)), garnet crystals nucleated after a ~35 ˚C overstep (Dragovic et al. 2018) and then grew up to ~2.5 cm in diameter in 3.8 ± 2.2 Myr during regional metamorphism (Gatewood et al. 2015). In the Cascades Crystalline Core, garnet experienced ~30-40ºC of overstepping and then grew over a period of < 6 Myr (Stowell et al. 2011). Thus, it appears that examples with extreme overstepping may subsequently result in very rapid garnet growth, while moderate overstepping results in slower garnet growth rates. This follows from the fact that nucleation rate is a function of the amount of temperature overstep and that the kinetics of intergranular transport are dependent on the absolute temperature of the system (e.g. Waters & Lovegrove 2002). Thus, if a

system is overstepped at high temperature, eventual crystal nucleation will be followed by efficient transport to the nuclei. This link between overstepping and the duration of garnet growth has potentially important implications for understanding the pulsed or continuous nature of metamorphism and its associated fluid generation.

In the minimally overstepped examples, there is an immediate difference in the chemical potential of all components at garnet-in. In the more significantly overstepped examples, there is an 'area' of *P-T* space in which $\Delta\mu_{Al2O3} = 0$, but garnet is nominally stable. Thus, the calculation of chemical potentials in the TEC and MSC may be used as a first order approximation to assess whether a rock experienced substantially overstepped garnet-in reactions.

Much of the previous discussion about overstepped garnet nucleation and growth has focused on improving methodologies to determine the *P-T* of garnet nucleation and comparing and contrasting the *P-T* of garnet nucleation constrained by different methodologies. Our work highlights that this discussion of overstepping must also include: i) consideration of the factors controlling the position of garnet-in curves, and ii) interrogation of additional information inherent in pseudosection calculations.

The garnet-in curve is generally defined as the *P-T* at which garnet first becomes thermodynamically stable in the TEC. Alternatively, we can explore the consequences of approximating garnet-in as the *P-T* at which $\Delta\mu_{Al2O3} \neq 0$. If that were the case, then all of the overstepped examples explored here would have lower apparent oversteps. For the three examples (Eastern Vermont, Central Himalaya, Funeral Mountains) in which $\Delta\mu_{Al2O3} \neq 0$ aligns with the *P-T* at which the garnet core isopleths intersect, this would lead to an interpretation that those rocks are not overstepped.

In many of our examples, the modal abundance of garnet calculated at *P-T* conditions immediately greater than garnet-in is < 0.5%. It is unclear if this would always be detected in a thin section point count (see Howarth (1998) for a discussion on the likely probabilities and errors associated with point counting). This leads to an interesting discrepancy between field, petrographic, and pseudosection calculations. For example, in the Nelson Aureole, Pattison & Tinkham (2009) calculate initial garnet stability in the pseudosection to be at 527ºC. Based on thermal modelling of the Nelson Batholith and associated contact aureole, this should occur 2300 meters from the batholith. However, the isograd is mapped in the field (based on the first visible presence of garnet) at 1400 meters from the batholith. Thus, there are 900 meters (equating to 30ºC) of section in which garnet has been calculated to be thermodynamically stable, but has not been recognized in the field or in thin section. Our pseudosection recalculations for this locality suggest that rocks would only contain 0.5% garnet by volume at *P-T* conditions immediately greater than garnet-in. This may not be readily detected without study of numerous thin sections and hand specimens, and in many cases it may thus be more appropriate to redefine an 'effective garnet-in' as the *P-T* conditions at which a more substantial garnet fraction would be stable.

## Acknowledgements

ABN acknowledges funding from the Virginia Tech ICTAS Doctoral Scholars Program. BD and MJC acknowledge support from NSF award OIA 1545903 (to M. Kohn, S. Penniston-Dorland, and M. Feineman). Harold Stowell, Oliver Wolfe, Jacob Forshaw, and an anonymous reviewer are thanked for constructive and helpful reviews. We thank Callum Hetherington for his handling of this paper as Associate Editor and David Pattison is thanked for comments on an earlier version of this manuscript. Members of the Metamorphic Processes Group at Virginia Tech are

684 thanked for discussions on this project and Victor Guevara and Calvin Mako are thanked for
685 detailed comments.

686

687 **References**

688 Ague, J.J., and Carlson, W.D. (2013) Metamorphism as garnet sees it: The kinetics of nucleation
689 and growth, equilibration, and diffusional relaxation. Elements, 9, 439–445.
690 Anczkiewicz, R., Chakraborty, S., Dasgupta, S., Mukhopadhyay, D., and Kołtonik, K. (2014)
691 Timing, duration and inversion of prograde Barrovian metamorphism constrained by high
692 resolution Lu-Hf garnet dating: A case study from the Sikkim Himalaya, NE India. Earth
693 and Planetary Science Letters, 407, 70–81.
694 Baxter, E.F., and Scherer, E.E. (2013) Garnet geochronology: Timekeeper of
695 tectonometamorphic processes. Elements, 9, 433–438.
696 Baxter, E.F., Caddick, M.J., and Dragovic, B. (2017) Garnet: A Rock-Forming Mineral
697 Petrochronometer. Reviews in Mineralogy &Geochemistry, 83, 469–533.
698 Bell, T.H., Rieuwers, M.T., Cihan, M., Evans, T.P., Ham, A.P., and Welch, P.W. (2013) Inter-
699 relationships between deformation partitioning, metamorphism and tectonism.
700 Tectonophysics, 587, 119–132.
701 Berman, R.G. (1988) Internally consistent thermodynamic data for minerals in the system Na2O-
702 K2O-CaO-MgO-FeO-Fe2O-SiO2-TiO2-H2O-CO2. Journal of Petrology, 29, 445–552.
703 Caddick, M.J., and Thompson, A.B. (2008) Quantifying the tectono-metamorphic evolution of
704 pelitic rocks from a wide range of tectonic settings: Mineral compositions in equilibrium.
705 Contributions to Mineralogy and Petrology, 156, 177–195.
706 Caddick, M.J., Bickle, M.J., Harris, N.B.W., Holland, T.J.B., Horstwood, M.S.A., Parrish, R.R.,

and Ahmad, T. (2007) Burial and exhumation history of a Lesser Himalayan schist: Recording the formation of an inverted metamorphic sequence in NW India. Earth and Planetary Science Letters, 264, 375–390.

Caddick, M.J., Konopásek, J., and Thompson, A.B. (2010) Preservation of garnet growth zoning and the duration of prograde metamorphism. Journal of Petrology, 51, 2327–2347.

Carlson, W.D. (1989) The significance of intergranuar diffusion to the mechanisms and kinetics of porphyroblast crystallization. Contribution to Mineralogy and Petrology, 103, 1–24.

——— (2002) Scales of disequilibrium and rates of equilibration during metamorphism. American Mineralogist, 87, 185–204.

——— (2010) Dependence of reaction kinetics on H2O activity as inferred from rates of intergranular diffusion of aluminium. Journal of Metamorphic Geology, 28, 735–752.

——— (2011) Porphyroblast crystallization: linking processes, kinetics, and microstructures. International Geology Review, 53, 406–445.

Carlson, W.D., Pattison, D.R.M., and Caddick, M.J. (2015a) Beyond the equilibrium paradigm: How consideration of kinetics enhances metamorphic interpretation. American Mineralogist, 100, 1659–1667.

Carlson, W.D., Hixon, J.D., Garber, J.M., and Bodnar, R.J. (2015b) Controls on metamorphic equilibration: the importance of intergranular solubilities mediated by fluid composition. Journal of Metamorphic Geology, 33, 123–146.

Carmichael, D.M. (1969) On the mechanism of prograde metamorphic reactions in quartz-bearing pelitic rocks. Contributions to Mineralogy and Petrology, 20, 244–267.

Castro, A.E., and Spear, F.S. (2016) Reaction overstepping and re-evaluation of peak P–T conditions of the blueschist unit Sifnos, Greece: implications for the Cyclades subduction

730 zone. International Geology Review, 59, 1–15.
731 Chernoff, C.B., and Carlson, W.D. (1997) Disequilibrium for Ca during growth of pelitic garnet.
732 Journal of Metamorphic Geology, 15, 421–438.
733 ——— (1999) Trace element zoning as a record of chemical disequilibrium during garnet
734 growth. Geology, 27, 555–558.
735 Christian, J.W. (1975) The Theory of Transformations in Metals and Alloys, 1–586 p. Pergamon
736 Press.
737 Coggon, R., and Holland, T.J.B. (2002) Mixing properties of phengitic micas and revised garnet-
738 phengite thermobarometers. Journal of Metamorphic Geology, 20, 683–696.
739 Connolly, J.A.D. (1990) Multivariable phase diagrams: an algorithm based on generalized
740 thermodynamics. American Journal of Science, 290, 666–718.
741 Connolly, J.A.D. (2005) Computation of phase equilibria by linear programming: A tool for
742 geodynamic modeling and its application to subduction zone decarbonation. Earth and
743 Planetary Science Letters, 236, 524–541.
744 Connolly, J.A.D., and Kerrick, D.M. (1987) An algorithm and computer program for calculating
745 composition phase diagrams. CALPHAD, 11, 1–55.
746 Craddock Affinati, S., Hoisch, T.D., Wells, M.L., and Vervoort, J.D. (2020) Pressure-
747 temperature-time paths from the Funeral Mountains, California, reveal Jurassic retroarc
748 underthrusting during early Sevier orogenesis. GSA Bulletin, 132, 1–19.
749 Dasgupta, S., Chakraborty, S., and Neogi, S. (2009) Petrology of an inverted Barrovian sequence
750 of metapelites in Sikkim Himalaya, India: Constraints on the tectonics of inversion.
751 American Journal of Science, 309, 43–84.
752 Dragovic, B., Samanta, L.M., Baxter, E.F., and Selverstone, J. (2012) Using garnet to constrain

753 the duration and rate of water-releasing metamorphic reactions during subduction: An
754 example from Sifnos, Greece. Chemical Geology, 314–317, 9–22.
755 Dragovic, B., Baxter, E.F., and Caddick, M.J. (2015) Pulsed dehydration and garnet growth
756 during subduction revealed by zoned garnet geochronology and thermodynamic modeling,
757 Sifnos, Greece. Earth and Planetary Science Letters, 413, 111–122.
758 Dragovic, B., Gatewood, M.P., Baxter, E.F., and Stowell, H.H. (2018) Fluid production rate
759 during the regional metamorphism of a pelitic schist. Contributions to Mineralogy and
760 Petrology, 173, 1–16.
761 Duchêne, S., Blichert-Toft, J., Luais, B., Télouk, P., Lardeaux, J.M., and Albarède, F. (1997) The
762 Lu-Hf dating of garnets and the ages of the Alpine high-pressure metamorphism. Nature,
763 387, 586–589.
764 Eskola, P. (1915) On the relations between the chemical and mineralogical composition in the
765 metamorphic rocks of the Orijarvi region. Bull. Comm. Geol. Finlande.
766 ——— (1920) The mineral facies of rocks. Norsk. Geol. Tidsskr., 6, 143–194.
767 Essene, E.J. (1982) Geologic thermometry and barometry. In Characterization of Metamorphism
768 through Mineral Equilbria: Mineralogical Society of America pp. 153–206.
769 Etzel, T.M., Catlos, E.J., Ataktürk, K., Lovera, O.M., Kelly, E.D., Çemen, I., and Diniz, E.
770 (2019) Implications for thrust-related shortening punctuated by extension from P-T paths
771 and geochronology of garnet-bearing schists, southern (Çine) Menderes Massif, SW
772 Turkey. Tectonics, 38, 1974–1998.
773 Evans, T.P. (2004) A method for calculating effective bulk composition modification due to
774 crystal fractionation in garnet-bearing schist: Implications for isopleth thermobarometry.
775 Journal of Metamorphic Geology, 22, 547–557.

776 Ferry, J.M., and Spear, F.S. (1978) Experimental calibration of the partitioning of Fe and Mg
777 between biotite and garnet. Contributions to Mineralogy and Petrology, 66, 113–117.
778 Fisher, G.W. (1978) Rate laws in metamorphism. Geochimica et Cosmochimica Acta, 42, 1035–
779 1050.
780 Florence, F.P., and Spear, F.S. (1991) Effects of diffusional modification of garnet growth
781 zoning on P-T path calculations. Contributions to Mineralogy and Petrology, 107, 487–500.
782 Fuhrman, M.L., and Lindsley, D.H. (1988) Ternary-feldspar modeling and thermometry.
783 American Mineralogist, 73, 201–215.
784 Fyfe, W.S., Turner, F.J., and Verhoogen, J. (1958) Kinetics of Metamorphic Reactions. In
785 Metamorphic Reactions and Metamorphic Facies p. 80. Geological Society of America.
786 Gaidies, F., Krenn, E., De Capitani, C., and Abart, R. (2008) Coupling forward modelling of
787 garnet growth with monazite geochronology: An application to the Rappold Complex
788 (Austroalpine crystalline basement). Journal of Metamorphic Geology, 26, 775–793.
789 Gaidies, F., Pattison, D.R.M., and de Capitani, C. (2011) Toward a quantitative model of
790 metamorphic nucleation and growth. Contributions to Mineralogy and Petrology, 162, 975–
791 993.
792 Gaidies, F., Petley-Ragan, A., Chakraborty, S., Dasgupta, S., and Jones, P. (2015) Constraining
793 the conditions of Barrovian metamorphism in Sikkim, India: P-T-t paths of garnet
794 crystallization in the Lesser Himalayan Belt. Journal of Metamorphic Geology, 33, 23–44.
795 Gatewood, M.P., Dragovic, B., Stowell, H.H., Baxter, E.F., Hirsch, D.M., and Bloom, R. (2015)
796 Evaluating chemical equilibrium in metamorphic rocks using major element and Sm-Nd
797 isotopic age zoning in garnet, Townshend Dam, Vermont, USA. Chemical Geology, 401,
798 151–168.

George, F.R., and Gaidies, F. (2017) Characterisation of a garnet population from the Sikkim Himalaya: insights into the rates and mechanisms of porphyroblast crystallisation. Contributions to Mineralogy and Petrology, 172, 1–22.

George, F.R., Gaidies, F., and Boucher, B. (2018) Population-wide garnet growth zoning revealed by LA-ICP-MS mapping: implications for trace element equilibration and syn-kinematic deformation during crystallisation. Contributions to Mineralogy and Petrology, 173, 1–24.

Ghent (1976) Plagioclase-garnet-Al2SiO5-quartz: a potential geobarometer-geothermometer. American Mineralogist, 61, 710–714.

Gibbs, J.W. (1928) Thermodynamics. Green Longmans, New York.

Green, E.C.R., White, R.W., Diener, J.F.A., Powell, R., Holland, T.J.B., and Palin, R.M. (2016) Activity–composition relations for the calculation of partial melting equilibria in metabasic rocks. Journal of Metamorphic Geology, 34, 845–869.

Groppo, C., Beltrando, M., and Compagnoni, R. (2009) The P-T path of the ultra-high pressure Lago Di Cignana and adjoining high-pressure meta-ophiolitic units: Insights into the evolution of the subducting Tethyan slab. Journal of Metamorphic Geology, 27, 207–231.

Guevara, V.E., and Caddick, M.J. (2016) Shooting at a moving target: Phase equilibria modelling of high-temperature metamorphism. Journal of Metamorphic Geology, 34, 209–235.

Hacker, B.R., Kirby, S.H., and Bohlen, S.R. (1992) Time and metamorphic petrology: Calcite to aragonite experiments. Science, 258, 110–112.

Hacker, B.R., Abers, G.A., and Peackcock, S.M. (2003) Subduction factory 1. Theoretical mineralogy, densities, seismic wave speeds, and H2O contents. Journal of Geophysical

822 Research, 108, 1–26.
823 Hernández-Uribe, D., and Palin, R.M. (2019) Catastrophic shear-removal of subcontinental
824 lithospheric mantle beneath the Colorado Plateau by the subducted Farallon slab. Scientific
825 Reports, 9, 1–10.
826 Hillert, M. (2008) Phase equilibria, phase diagrams, and phase transformations: their
827 thermodynamic basis, 2nd ed. Cambridge University Press, Cambridge.
828 Hillert, M., and Rettenmayr, M. (2003) Deviation from local equilibrium at migrating phase
829 interfaces. Acta Materialia, 51, 2803–2809.
830 Hodges, K.V., and McKenna, L.W. (1987) Realistic propagation of uncertainties in geologic
831 thermobarometry. American Mineralogist, 72, 671–680.
832 Hodges, K.V., and Spear, F.S. (1982) Geothermometry, geobarometry and the Al2SiO5 triple
833 point at Mt. Moosilauke, New Hampshire. American Mineralogist, 67, 1118–1134.
834 Holland, T.J.B., and Powell, R. (1998) An internally consistent thermodynamic data set for
835 phases of petrological interest. Journal of Metamorphic Geology, 16, 309–343.
836 ——— (2003) Activity-compositions relations for phases in petrological calculations: An
837 asymetric multicomponent formulation. Contributions to Mineralogy and Petrology, 145,
838 492–501.
839 ——— (2004) An internally consistent thermodynamic data set for phases of petrological
840 interest. Journal of Metamorphic Geology, 16, 309–343.
841 Holland, T.J.B., and Powell, R. (2011) An improved and extended internally consistent
842 thermodynamic dataset for phases of petrological interest, involving a new equation of state
843 for solids. Journal of Metamorphic Geology, 29, 333–383.
844 Holland, T.J.B., Baker, J., and Powell, R. (1998) Mixing properties and activity-composition

relationships of chlorites in the system MgO-FeO-Al2O3-SiO2-H2O. European Journal of Mineralogy, 10, 395–406.

Howarth, R.J. (1998) Improved point estimates of uncertainty in proportions, point-counting, and pass-fail test results. American Journal of Science, 298, 594–607.

Iaccarino, S., Montomoli, C., Carosi, R., Massonne, H.J., and Visonà, D. (2017) Geology and tectono-metamorphic evolution of the Himalayan metamorphic core: Insights from the Mugu Karnali transect, Western Nepal (Central Himalaya). Journal of Metamorphic Geology, 35, 301–325.

Joesten, R. (1977) Evolution of mineral assemblage zoning in diffusion metasomatism. Geochimica et Cosmochimica Acta, 41, 649–670.

Kelly, E.D., Carlson, W.D., and Ketcham, R.A. (2013a) Crystallization kinetics during regional metamorphism of porphyroblastic rocks. Journal of Metamorphic Geology, 31, 963–979.

——— (2013b) Magnitudes of departures from equilibrium during regional metamorphism of porphyroblastic rocks. Journal of Metamorphic Geology, 31, 981–1002.

Kelly, E.D., Hoisch, T.D., Wells, M.L., Vervoort, J.D., and Beyene, M.A. (2015) An Early Cretaceous garnet pressure–temperature path recording synconvergent burial and exhumation from the hinterland of the Sevier orogenic belt, Albion Mountains, Idaho. Contributions to Mineralogy and Petrology, 170, 1–22.

Kerrick, D.M., and Connolly, J.A.D. (2001) Metamorphic devolatilization of subducted oceanic metabasalts: Implications for seismicity, arc magmatism and volatile recycling. Earth and Planetary Science Letters, 189, 19–29.

Ketcham, R.A., and Carlson, W.D. (2012) Numerical simulation of diffusion-controlled nucleation and growth of porphyroblasts. Journal of Metamorphic Geology, 30, 489–512.

868 Konrad-Schmolke, M., Handy, M.R., Babist, J., and O'Brien, P.J. (2005) Thermodynamic
869 modelling of diffusion-controlled garnet growth. Contributions to Mineralogy and
870 Petrology.
871 Konrad-Schmolke, M., Babist, J., Handy, M.R., and O'Brien, P.J. (2006) The physico-chemical
872 properties of a subducted slab from garnet zonation patterns (Sesia Zone, western Alps).
873 Journal of Petrology, 47, 2123–2148.
874 Kretz, R. (1966) Interpretation of the shape of mineral grains in metamorphic rocks. Journal of
875 Petrology, 7, 68–94.
876 Kretz, R. (1974) Some models for the rate of crystallization of garnet in metamorphic rocks.
877 Lithos, 7, 123–131.
878 Lanari, P., and Duesterhoeft, E. (2019) Modeling metamorphic rocks using equilibrium
879 thermodynamics and internally consistent databases: Past achievements, problems and
880 perspectives. Journal of Petrology, 60, 19–56.
881 Lanari, P., and Engi, M. (2017) Local bulk composition effects on metamorphic mineral
882 assemblages. Reviews in Mineralogy & Geochemistry, 83, 55–93.
883 Lanari, P., Wagner, T., and Vidal, O. (2014) A thermodynamic model for di-trioctahedral
884 chlorite from experimental and natural data in the system MgO-FeO-Al2O3-SiO2-H2O:
885 applications to P-T sections and geothermometry. Contributions to Mineralogy and
886 Petrology, 167, 1–19.
887 Lasaga, A.C. (1986) Metamorphic reaction rate laws and development of isograds. Mineralogical
888 Magazine, 50, 359–373.
889 Lasaga, A.C., and Rye, D.M. (1993) Fluid flow and chemical kinetics in metamorphic systems.
890 American Journal of Science, 293, 361–404.

Liu, M., and Yund, R.A. (1993) Transformation kinetics of polycrystalline aragonite to calcite: New experimental data, modelling, and implications. Contributions to Mineralogy and Petrology, 114, 465–478.

Mahar, E.M., Baker, J.M., Powell, R., Holland, T.J.B., and Howell, N. (1997) The effect of Mn on mineral stability in metapelites. Journal of Metamorphic Geolgoy, 15, 223–238.

Manning, C.E. (2007) Solubility of corundum + kyanite in H2O at 700°C and 10 kbar: Evidence for Al-Si complexing at high pressure and temperature. Geofluids, 7, 258–269.

Marmo, B.A., Clarke, G.L., and Powell, R. (2002) Fractionation of bulk rock composition due to porphyroblast growth: Effects on eclogite facies mineral equilibria, Pam Peninsula, New Caledonia. Journal of Metamorphic Geology, 20, 151–165.

McCarron, T., Gaidies, F., McFarlane, C.R.M., Easton, R.M., and Jones, P. (2014) Coupling thermodynamic modeling and high-resolution in situ LA-ICP-MS monazite geochronology: evidence for Barrovian metamorphism late in the Grenvillian history of southeastern Ontario. Mineralogy and Petrology, 108, 741–758.

McCarron, T., McFarlane, C.R.M., and Gaidies, F. (2019) The significance of Mn-rich ilmenite and the determination of P-T paths from zoned garnet in metasedimentary rocks from the western Cape Breton Highlands, Nova Scotia. Journal of Metamorphic Geology, 37, 1171–1192.

Menard, T., and Spear, F.S. (1994) Metamorphic P-T paths from calcic pelitic schists from the Strafford Dome, Vermont, USA. Journal of Metamorphic Geology, 12, 811–826.

Milke, R., and Heinrich, W. (2002) Diffusion-controlled growth of wollastonite rims between quartz and calcite: Comparison between nature and experiment. Journal of Metamorphic Geology, 20, 467–480.

914 Moynihan, D.P., and Pattison, D.R.M. (2013) An automated method for the calculation of P-T
915 paths from garnet zoning, with application to metapelitic schist from the Kootenay Arc,
916 British Columbia, Canada. Journal of Metamorphic Geology, 31, 525–548.
917 Mullin (1992) Crystallization, 3rd ed. Butterworth, Heinemann, Oxford.
918 Newton, R.C., and Manning, C.E. (2007) Solubility of grossular, Ca3Al2Si3O12, in H2O-NaCl
919 solutions at 800 °C and 10 kbar, and the stability of garnet in the system CaSiO3-Al2O3-
920 H2O-NaCl. Geochimica et Cosmochimica Acta, 71, 5191–5202.
921 Nielsen, A.E. (1964) Kinetics of Precipitation. Pergamon Press.
922 Palin, R.M., Weller, O.M., Waters, D.J., and Dyck, B. (2016) Quantifying geological uncertainty
923 in metamorphic phase equilibria modelling; A Monte Carlo assessment and implications for
924 tectonic interpretations. Geoscience Frontiers, 7, 591–607.
925 Pattison, D.R.M., and DeBuhr, C.L. (2015) Petrology of metapelites in the Bugaboo aureole,
926 British Columbia, Canada. Journal of Metamorphic Geology, 33, 437–462.
927 Pattison, D.R.M., and Spear, F.S. (2018) Kinetic control of staurolite-Al2SiO5mineral
928 assemblages: Implications for Barrovian and Buchan metamorphism. Journal of
929 Metamorphic Geology, 36, 667–690.
930 Pattison, D.R.M., and Tinkham, D.K. (2009) Interplay between equilibrium and kinetics in
931 prograde metamorphism of pelites: an example from the Nelson aureole, British Columbia.
932 Journal of Metamorphic Geology, 27, 249–279.
933 Pattison, D.R.M., and Vogl, J.J. (2005) Contrasting sequences of metapelitic mineral-
934 assemblages in the aureole of the tilted Nelson Batholith, British Columbia: Implications for
935 phase equilibria and pressure determination in andalusite-sillimanite-type settings. Canadian
936 Mineralogist, 43, 51–88.

Pattison, D.R.M., de Capitani, C., and Gaidies, F. (2011) Petrological consequences of variations in metamorphic reaction affinity. Journal of Metamorphic Geology, 29, 953–977.

Pollington, A.D., and Baxter, E.F. (2010) High resolution Sm-Nd garnet geochronology reveals the uneven pace of tectonometamorphic processes. Earth and Planetary Science Letters, 293, 63–71.

Powell, R. (1978) Equilibrium Thermodynamics in Petrology: An Introduction, 1–294 p. Harper & Row Publishers, New York.

Powell, R., and Holland, T.J.B. (1999) Relating formulations of the thermodynamics of mineral solid solutions: Activity modeling of pyroxenes, amphiboles, and micas. American Mineralogist, 84, 1–14.

Powell, R., and Holland, T.J.B. (2008) On thermobarometry. Journal of Metamorphic Geolgoy, 26, 155–179.

Powell, R., Holland, T.J.B., and Worley, B. (1998) Calculating phase diagrams involving solid solutions via non-linear equations, with examples using THERMOCALC. Journal of Metamorphic Geology, 16, 577–588.

Powell, R., White, R.W., Green, E.C.., Holland, T.. B., and Diener, J.F.. (2014) On parameterizing thermodynamic descriptions of minerals for petrological calculations. Journal of Metamorphic Geology, 32, 245–260.

Powell, R., Evans, K.A., Green, E.C.R., and White, R.W. (2019) The truth and beauty of chemical potentials. Journal of Metamorphic Geology, 37, 1007–1019.

Ridley, J., and Thompson, A.B. (1986) The role of mineral kinetics in the development of metamorphic microtextures. Advances in Physical Geochemistry, 5, 154–193.

Rimstidt, J.D. (2014) Geochemical Rate Models. Cambridge University Press, New York.

960 Rubie, D.C. (1986) The catalysis of mineral reactions by water and restrictions on the presence
961 of aqueous fluid during metamorphism. Mineralogical Magazine, 50, 399–415.
962 ——— (1998) Disequilibrium during metamorphism: The role of nucleation kinetics. Geological
963 Society, London, Special Publications, 138, 199–214.
964 Rubie, D.C., Tsuchida, Y., Yagi, T., Utsumi, W., Kikegawa, T., Shimomura, O., and Brearley,
965 A.J. (1990) An in situ X ray diffraction study of the kinetics of the Ni2SiO4 olivine-spinel
966 transformation. Journal of Geophysical Research, 95, 15829–15844.
967 Rumble, D. (1976) The use of mineral solid solutions to measure chemical potential gradients.
968 American Mineralogist, 61, 1167–1174.
969 Scherer, E.E., Cameron, K.L., and Blichert-Toft, J. (2000) Lu-Hf garnet geochronology: Closure
970 temperature relative to the Sm-Nd system and the effects of trace mineral inclusions.
971 Geochimica et Cosmochimica Acta, 64, 3413–3432.
972 Seman, S., Stockli, D.F., and McLean, N.M. (2017) U-Pb geochronology of grossular-andradite
973 garnet. Chemical Geology, 460, 106–116.
974 Spear, F.S. (1988) Metamorphic fractional crystallization and internal metasomatism by
975 diffusional homogenization of zoned garnets. Contributions to Mineralogy and Petrology,
976 99, 507–517.
977 Spear, F.S. (1993) Metamorphic Phase Equilibria and Pressure-Temperature-Time Paths.
978 Mineralogical Society of America, Washington, DC.
979 Spear, F.S., and Pyle, J.M. (2010) Theoretical modeling of monazite growth in a low-Ca
980 metapelite. Chemical Geology, 273, 111–119.
981 Spear, F.S., and Selverstone, J. (1983) Quantitative P-T paths from zoned minerals: Theory and
982 tectonic applications. Contributions to Mineralogy and Petrology, 83, 348–357.

983 Spear, F.S., and Wolfe, O.M. (2018) Evaluation of the effective bulk composition (EBC) during
984 growth of garnet. Chemical Geology, 491, 39–47.
985 Spear, F.S., Selverstone, J., Hickmott, D., Crowley, P., and Hodges, K.V. (1984) P-T paths from
986 garnet zoning: A new technique for deciphiering tectonic process in crystalline terranes.
987 Geology, 12, 87–90.
988 Spear, F.S., Thomas, J.B., and Hallett, B.W. (2014) Overstepping the garnet isograd: A
989 comparison of QuiG barometry and thermodynamic modeling. Contributions to Mineralogy
990 and Petrology, 168.
991 St-Onge, M.R. (1987) Zoned poikiloblastic garnets: P-T paths and syn-metamorphic uplift
992 through 30 km of structural depth, Wopmay Orogen, Canada. Journal of Petrology, 28, 1–
993 21.
994 Starr, P.G., Pattison, D.R.M., and Ames, D.E. (2020) Mineral assemblages and phase equilibria
995 of metabasites from the prehnite–pumpellyite to amphibolite facies, with the Flin Flon
996 Greenstone Belt (Manitoba) as a type example. Journal of Metamorphic Geology, 38, 71–
997 102.
998 Stipska, P., Powell, R., White, R.W., and Baldwin, J.A. (2010) Using calculated chemical
999 potential relationships to account for coronas around kyanite: An example from the
1000 Bohemian Massif. Journal of Metamorphic Geology, 28, 97–116.
1001 Stowell, H., Bulman, G., Tinkham, D., and Zuluaga, C. (2011) Garnet growth during crustal
1002 thickening in the Cascades Crystalline Core, Washington, USA. Journal of Metamorphic
1003 Geology, 29, 627–647.
1004 Symmes, G.H., and Ferry, J.M. (1992) The effect of whole-rock MnO content on the stability of
1005 garnet in pelitic schists during metamorphism. Journal of Metamorphic Geology, 10, 221–

237.

Thompson, C.V., and Spaepen, F. (1983) Homogeneous crystal nucleation in binary metallic melts. Acta Metall., 31, 2021–2027.

Thompson, J.B. (1957) The graphical analysis of mineral assemblages in pelitic schists. American Mineralogist, 42, 841–858.

Tinkham, D.K., and Ghent, E.D. (2005) Estimating P-T conditions of garnet growth with isochemical phase-diagram sections and the problem of effective bulk-composition. Canadian Mineralogist, 43, 35–50.

Tinkham, D.K., Zuluaga, C.A., and Stowell, H.H. (2001) Metapelite phase equilibria modeling in MnNCKFMASH: The effect of variable Al2O3 and MgO/(MgO+FeO) on mineral stability. Geological Materials Research, 3, 1–42.

Tomkins, H.S., and Pattison, D.R.M. (2007) Accessory phase petrogenesis in relation to major phase assemblages in pelites from the Nelson contact aureole, southern British Columbia. Journal of Metamorphic Geology, 25, 401–421.

Tracy, R.J. (1982) Compositional zoning and inclusions in metamorphic minerals. Characterization of Metamorphism through Mineral Equilbria: Mineralogical Society of America, 10, 355–397.

Tracy, R.J., Robinson, P., and Thompson, A.B. (1976) Garnet composition and zoning in the determination of temperatuer and pressure of metamorphism, central Massachusetts. American Mineralogist, 61, 762–775.

Vidal, O. (1999) Calibration and testing of an empirical chloritoid-chlorite Mg-Fe thermometer and thermodynamic data for daphnite. Journal of Metamorphic Geology, 17, 25–39.

Walther, J. V., and Wood, B.J. (1984) Rate and mechanism in prograde metamorphism.

1029 Contributions to Mineralogy and Petrology, 88, 246–259.
1030 Waters, D.J. (2019) Metamorphic constraints on the tectonic evolution of the High Himalaya in
1031 Nepal: the art of the possible. Geological Society, London, Special Publications, 483, 325–
1032 375.
1033 Waters, D.J., and Lovegrove, D.P. (2002) Assessing the extent of disequilibrium and
1034 overstepping of prograde metamorphic reactions in metapelites from the Bushveld Complex
1035 aureole, South Africa. Journal of Metamorphic Geology, 20, 135–149.
1036 Weller, O.M., St-Onge, M.R., Waters, D.J., Rayner, N., Searle, M.P., Chung, S.L., Palin, R.M.,
1037 Lee, Y.H., and Xu, X. (2013) Quantifying Barrovian metamorphism in the Danba Structural
1038 Culmination of eastern Tibet. Journal of Metamorphic Geology, 31, 909–935.
1039 White, R.W., and Powell, R. (2002) Melt loss and the preservation of granulite facies mineral
1040 assemblages. Journal of Metamorphic Geology, 20, 621–632.
1041 White, R.W., Powell, R., and Baldwin, J.A. (2008) Calculated phase equilibria involving
1042 chemical potentials to investigate the textural evolution of metamorphic rocks. Journal of
1043 Metamorphic Geology, 26, 181–198.
1044 White, R.W., Powell, R., Holland, T.J.B., Johnson, T.E., and Green, E.C.R. (2014a) New
1045 mineral activity-composition relations for thermodynamic calculations in metapelitic
1046 systems. Journal of Metamorphic Geology, 32, 261–286.
1047 White, R.W., Powell, R., and Johnson, T.E. (2014b) The effect of Mn on mineral stability in
1048 metapelites revisited: new a-x relations for manganese-bearing minerals. Journal of
1049 Metamorphic Geology, 32, 809–828.
1050 Whitney, D.L., and Evans, B.W. (2010) Abbreviations for names of rock-forming minerals.
1051 American Mineralogist, 95, 185–187.

1052 Wilbur, D.E., and Ague, J.J. (2006) Chemical disequilibrium during garnet growth: Monte Carlo
1053 simulations of natural crystal morphologies. Geology, 34, 689–692.
1054 Wolfe, O.M., and Spear, F.S. (2018) Determining the amount of overstepping required to
1055 nucleate garnet during Barrovian regional metamorphism, Connecticut Valley
1056 Synclinorium. Journal of Metamorphic Geology, 36, 79–94.
1057 Wood, B.J., and Walther, J. V. (1983) Rates of hydrothermal reactions. Science, 222, 413–415.
1058 Yardley, B.W.D. (1978) Genesis of the Skagit Gneiss migmatites, Washington, and the
1059 distinction between possible mechanisms of migmatization. Geological Society of America
1060 Bulletin, 89, 941–951.
1061 Zeh, A., and Holness, M.B. (2003) The effect of reaction overstep on garnet microtextures in
1062 metapelitic rocks of the Ilesha Schist Belt, SW Nigeria. Journal of Petrology, 44, 967–991.
1063 Zuluaga, C., Stowell, H.H., and Tinkham, D.K. (2005) The effect of zoned garnet on metapelite
1064 pseudosection topology and calculated metamorphic P-T paths. American Mineralogist, 90,
1065 1619–1628.
1066

1067 **Figure Captions**

1068 **Figure 1:** Overview of the methodologies applied in this paper. A. Schematic TEC
1069 pseudosection for a theoretical pseudosection (hypothetical bulk composition), with mineral
1070 abbreviations from Whitney & Evans (2010). Bold dashed line indicates the bounds of garnet
1071 stability. Compositional isopleths corresponding to measured garnet core compositions are
1072 shown in green ($X_{sps}$), yellow ($X_{grs}$), red ($X_{alm}$), and blue ($X_{prp}$). Maroon hexagon indicates the
1073 intersection of the garnet core isopleths and thus apparent garnet nucleation. Arrow represents
1074 the shortest vector from garnet-in to this *P-T* condition. B. MSC pseudosection for the same

hypothetical bulk composition, yielding an identical assemblage but without garnet. C. Free-energy–composition (*G*-*X*) diagram showing stable minerals X and Z and the tangent that defines the chemical potentials of MgO and FeO in a two-component system. D: *G*-*X* diagram showing stable minerals W, X and Z and the tangent plane in a three-component system. E: Differences in the chemical potential of oxide components between the calculations shown in A and B along the *P*-*T* path shown. in A and B (i.e. $\Delta\mu_{MgO} = \mu_{MgO\ TEC} - \mu_{MgO\ MSC}$).

**Figure 2:** A. TEC pseudosection for sample 24-99 (Sikkim, Himalaya) calculated with ds5.5. B. MSC pseudosection for sample 24-99. C. $\Delta\mu_{component}$ along the *P*-*T* path shown in A & B. D. TEC pseudosection for sample 24-99 (Sikkim, Himalaya) calculated with ds6.2. E. MSC pseudosection for sample 24-99. C. $\Delta\mu_{component}$ along the *P*-*T* path shown in D & E.

**Figure 3:** A. TEC pseudosection for sample 35F03 (Rappold Complex) calculated with ds5.5. B. MSC pseudosection for sample 35F03. C. $\Delta\mu_{component}$ along the *P*-*T* path shown in A & B.

**Figure 4:** A. TEC pseudosection for sample TM549A (Eastern Vermont) calculated with ds5.5. B. MSC pseudosection for sample TM549A. C. $\Delta\mu_{component}$ along *P*-*T* path #1 shown in A & B. D. $\Delta\mu_{component}$ along *P*-*T* path #2 shown in A & B.

**Figure 5:** A. TEC pseudosection for sample AV26A (Pomfret Dome) calculated with ds5.5. B. MSC pseudosection for sample AV26A. C. $\Delta\mu_{component}$ along the *P*-*T* path shown in A & B. D. TEC pseudosection for sample AV26A (Pomfret Dome) calculated with ds6.2. E. MSC pseudosection for sample AV26A. F. $\Delta\mu_{component}$ along the *P*-*T* path shown in A & B.

**Figure 6:** A. TEC pseudosection for sample 93-CW-4 (Nelson Aureole), calculated with ds5.5. B. MSC pseudosection for sample 93-CW-4. C-G. $\Delta\mu_{MgO}$, $\Delta\mu_{MnO}$, $\Delta\mu_{FeO}$ $\Delta\mu_{CaO,}$ and $\Delta\mu_{Al2O3}$ as functions of *P* and *T*. H. $\Delta\mu_{component}$ along the heating path shown in A-G.

**Figure 7:** A. TEC pseudosection for sample 93-CW-04 (Nelson Aureole) calculated with ds6.2. B. MSC pseudosection for sample 93-CW-04. C. $\Delta\mu_{component}$ along the *P*-*T* path shown in A & B.

**Figure 8:** A: Schematic three component *G*-*X* diagram at *P*-*T* conditions where garnet is not stable in the TEC. Gray triangle is the tangent plane through stable phases whose *G*-*X* surfaces have been removed for clarity. B. *G*-*X* diagram at *P*-*T* conditions where garnet is stable in the TEC but has been prohibited in the MSC (yellow tangent plane). $\mu_{MgO}$ and $\mu_{FeO}$ are different between the TEC and MSC but $\Delta\mu_{Al2O3}$ is the same in each. C. Further increase in $\Delta\mu_{MgO}$ and $\Delta\mu_{FeO}$ without developing $\Delta\mu_{Al2O3}$. D. A *G*-*X* diagram for *P*-*T* conditions at which the chemical potentials of all three components differ between the TEC and MSC.

**Figure 9:** A. $T$-$X_{MnO}$ TEC diagram for sample AV26A at $P$ = 5.0 kbar. $X$ axis ranges from 0.0 wt% MnO to 0.2 wt% MnO. Dashed line denotes garnet-in. B. $T$-$X_{MnO}$ MSC diagram for sample AV26A at $P$ = 5.0 kbar. C. $T$-$X_{MnO}$ diagram contoured for $\Delta\mu_{Al2O3}$ (J/mol).

**Table 1:** Comparison of amount of overstepping reported in the literature and that calclated in this ds5.5 thermodynamic dataset. ** = sample described in main text. * =sample described in Supple

| | | | **Reported in the Literature** | |
|---|---|---|---|---|
| Location | Sample # | Original Source | *P-T* of Garnet Nucleation | Amount of Apparent Overstep |
| | | | **Examples with Minimal Overstepping (<10ºC and 0.5** | |
| Sikkim, Himalaya ** | 24-99 | Gaidies et al. 2015 | 520ºC 4.5 kbar | 0ºC 0 kbar |
| Rappold Complex ** | 35F03 | Gaidies et al. 2008 | 530ºC 5.2 kbar | 0ºC 0 kbar |
| Eastern Tibet * | W122 | Weller et al. 2013 | not reported | not reported |
| Kootenary Arc * | DM_06_128 | Moyniham & Pattison 2013 | 500ºC 5.2 kbar | <10ºC <0.5 kbar |
| | | | **Examples with Apparent Overstepping (>10ºC and 0** | |
| Eastern Vermont ** | TM549a | Spear et al. 2014 | 540ºC 8.0 kbar | 10ºC 0.6 kbar |
| Pomfret Dome ** | AV26A | Bell et al. 2013 | 550ºC 8.0 kbar | 30ºC 1.5 kbar |
| Nelson Aureole ** | 93-CW-4 | Gaidies et al. 2011 | 545ºC 3.5 kbar | 30ºC 0 kbar |
| Southeastern Ontario * | 12TM16 | McCarron et al. 2014 | 512ºC 4.0 kbar | 32ºC 1.1 kbar |
| Southwest Turkey * | ED34 | Etzel et al. 2019 | 565ºC 6.0 kbar | 25ºC 0.8 kbar |
| Central Himalaya * | D13-75 | Iaccarino et al. 2017 | 520ºC 5.5 kbar | 30ºC 0.7 kbar |
| Albion Mountains * | TH203B | Kelly et al. 2015 | 550ºC 5.1 kbar | 50ºC 0.7 kbar |
| Funeral Mountains * | SSFM307-7G | Craddock-Affinati et al. 2020 | 550ºC 6.1 kbar | >50ºC >2 kbar |

s study using the THERMOCALC
mental Material

| This Study (ds5.5) | |
|---|---|
| *P-T* of Garnet Nucleation | Amount of Apparent Overstep |
| **5 kbar)** | |
| 526ºC 5.0 kbar | 0ºC 0 kbar |
| 531ºC 4.4 kbar | 0ºC 0 kbar |
| 547ºC 4.9 kbar | 0ºC 0 kbar |
| 491ºC 5.0 kbar | 4ºC 0.2 kbar |
| **.5 kbar)** | |
| 540ºC 5.8 kbar | 35ºC 1.5 kbar |
| 540ºC 7.4 kbar | 38ºC 2.3 kbar |
| 545ºC 3.5 kbar | 43ºC 0 kbar |
| 530ºC 4.4 kbar | 34ºC 1.0 kbar |
| 550ºC 6.3 kbar | 26ºC 1.2 kbar |
| 530ºC 5.4 kbar | 22ºC 1.0 kbar |
| 550ºC 6.3 kbar | 43ºC 1.9 kbar |
| 552ºC 7.1 kbar | 34ºC 1.7 kbar |

**Table 2**: Summary of Results for 12 Samples Calculated Using THERMOCALC ds5.5. ** = sample de

| Location | *P-T* of Garnet Isograd | *P-T* of Garnet Nucleation | Amount of Apparent Overstep | First Component(s) whose $\Delta\mu \neq 0$ |
|---|---|---|---|---|
| | | | **Examples with Minimal Overstepping** | |
| Sikkim, Himalaya ** | 526ºC 5.0 kbar | 526ºC 5.0 kbar | 0ºC 0 kbar | MnO, MgO, $Al_2O_3$, FeO |
| Rappold Complex ** | 531 ºC 4.4 kbar | 531ºC 4.4 kbar | 0ºC 0 kbar | MnO, MgO, $Al_2O_3$, FeO, CaO |
| Eastern Tibet * | 547ºC 4.9 kbar | 547ºC 4.9 kbar | 0ºC 0 kbar | MnO, MgO, FeO, CaO |
| Kootenary Arc * | 487ºC 4.8 kbar | 491ºC 5.0 kbar | 4ºC 0.2 kbar | MnO, MgO, FeO, CaO |
| | | | **Examples with Apparent Overstepping** | |
| Eastern Vermont ** | 505 ºC 4.3 kbar | 540ºC 5.8 kbar | 35ºC 1.5 kbar | MnO, MgO, CaO |
| Pomfret Dome ** | 502 ºC 5.1 kbar | 540ºC 7.4 kbar | 38ºC 2.3 kbar | MnO |
| Nelson Aureole ** | 502 ºC 3.5 kbar | 545ºC 3.5 kbar | 43ºC 0 kbar | MnO |
| Southeastern Ontario * | 496 ºC 3.4 kbar | 530ºC 4.4 kbar | 34ºC 1.0 kbar | MnO, MgO |
| Southwest Turkey * | 524 ºC 5.1 kbar | 550ºC 6.3 kbar | 26ºC 1.2 kbar | MnO, MgO |
| Central Himalaya * | 508 ºC 4.4 kbar | 530ºC 5.4 kbar | 22ºC 1.0 kbar | MnO, FeO, MgO, CaO |
| Albion Mountains * | 507 ºC 4.4 kbar | 550ºC 6.3 kbar | 43ºC 1.9 kbar | MnO, MgO, CaO |
| Funeral Mountains * | 518 ºC 5.4 kbar | 552ºC 7.1 kbar | 34ºC 1.7 kbar | MnO, MgO |

scribed in main text. * =sample described in Supplemental Material.

| *P-T* Conditions Where First $\Delta\mu_{component} \neq 0$ | $\Delta T$ & $\Delta P$ Between *P-T* of Garnet-in and *P-T* Where First Component(s) $\neq 0$ | Final Component(s) whose $\Delta\mu \neq 0$ | *P-T* Conditions Where Last $\Delta\mu_{component} \neq 0$ | $\Delta T$ & $\Delta P$ Between *P-T* of Garnet-in and *P-T* Where Last Component(s) $\neq 0$ |
|---|---|---|---|---|
| **g (<10ºC and 0.5 kbar)** | | | | |
| 526ºC 5.0 kbar | 0ºC 0 kbar | CaO | 530ºC 5.2 kbar | 4ºC 0.2 kbar |
| 531ºC 4.4 kbar | 0ºC 0 kbar | N/A | N/A | N/A |
| 547ºC 4.9 kbar | 0ºC 0 kbar | $Al_2O_3$ | 549ºC 4.9 kbar | 2ºC 0 kbar |
| 487ºC 4.8 kbar | 0ºC 0 kbar | $Al_2O_3$ | 492ºC 5.1 kbar | 5ºC 0.3 kbar |
| **ıg (>10ºC and 0.5 kbar)** | | | | |
| 505ºC 4.3 kbar | 0ºC 0 kbar | $Al_2O_3$ | 541ºC 5.8 kbar | 36ºC 1.5 kbar |
| 502ºC 5.1 kbar | 0ºC 0 kbar | $Al_2O_3$ | 530ºC 6.7 kbar | 28ºC 1.6 kbar |
| 502ºC 3.5 kbar | 0ºC 0 kbar | $Al_2O_3$ | 528ºC 3.5 kbar | 26ºC 0 kbar |
| 496ºC 3.4 kbar | 0ºC 0 kbar | $Al_2O_3$ | 513ºC 3.8 kbar | 17ºC 0.4 kbar |
| 524ºC 5.1 kbar | 0ºC 0 kbar | $Al_2O_3$, CaO | 532ºC 5.5 kbar | 8ºC 0.4 kbar |
| 508ºC 4.4 kbar | 0ºC 0 kbar | $Al_2O_3$ | 532ºC 5.5 kbar | 24ºC 1.1 kbar |
| 507ºC 4.4 kbar | 0ºC 0 kbar | $Al_2O_3$ | 532ºC 5.5 kbar | 25ºC 1.1 kbar |
| 518ºC 5.4 kbar | 0ºC 0 kbar | $Al_2O_3$ | 551ºC 7.0 kbar | 33ºC 1.6 kbar |

**Table 3:** Summary of Results for 5 Samples Calculated with THERMOCALC ds6.2 ** = sa

| Location | *P-T* of Garnet Isograd | *P-T* of Garnet Nucleation | Amount of Apparent Overstep | First Component(s) whose $\Delta\mu \neq 0$ |
|---|---|---|---|---|
| | | | **Examples with Minimal Overstepp** | |
| Sikkim, Himalaya ** | 522ºC 4.9 kbar | 525ºC 5.2 kbar | 3ºC 0.3 kbar | MnO, MgO |
| Rappold Complex * | 525ºC 4.4 kbar | 537ºC 4.9 kbar | 12ºC 0.5 kbar | MnO |
| | | | **Examples with Apparent Overstep** | |
| Eastern Vermont * | 505ºC 4.3 kbar | 550ºC 6.3 kbar | 45ªC 2.0 kbar | MnO |
| Pomfret Dome ** | 510ºC 5.5 kbar | 548ºC 7.8 kbar | 38ºC 2.3 kbar | MnO, MgO, CaO |
| Nelson Aureole ** | 443ºC 3.5 kbar | 545ºC 3.5 kbar | 102ºC 0 kbar | MnO, MgO |

nple described in main text. * =sample described in Supplemental Material.

| *P-T* Conditions Where First $\Delta\mu_{component} \neq 0$ | $\Delta T$ & $\Delta P$ Between *P-T* of Garnet-in and *P-T* Where First Component(s) $\neq 0$ | Final Component(s) whose $\Delta\mu \neq 0$ | *P-T* Conditions Where Last $\Delta\mu_{component} \neq 0$ |
|---|---|---|---|
| **ing (<10ºC and 0.5 kbar)** | | | |
| 522ºC 4.9 kbar | 0ºC 0 kbar | $Al_2O_3$ | 528ºC 5.5 kbar |
| 525ºC 4.4 kbar | 0ºC 0 kbar | $Al_2O_3$ | 541ºC 5.0 kbar |
| **ping (>10ºC and 0.5 kbar)** | | | |
| 505ºC 4.3 kbar | 0ºC 0 kbar | $Al_2O_3$ | 531ºC 5.4 kbar |
| 510ºC 5.5 kbar | 0ºC 0 kbar | $Al_2O_3$ | 520ºC 6.1 kbar |
| 443ºC 3.5 kbar | 0ºC 0 kbar | $Al_2O_3$ | 539ºC 3.5 kbar |

$\Delta T$ & $\Delta P$ Between *P-T*
of Garnet-in and *P-T*
Where Last
Component(s) $\neq 0$

6ºC 0.6 kbar

16ºC 0.6 kbar

26ºC 1.1 kbar

10ºC 0.6 kbar

96ºC 0 kbar

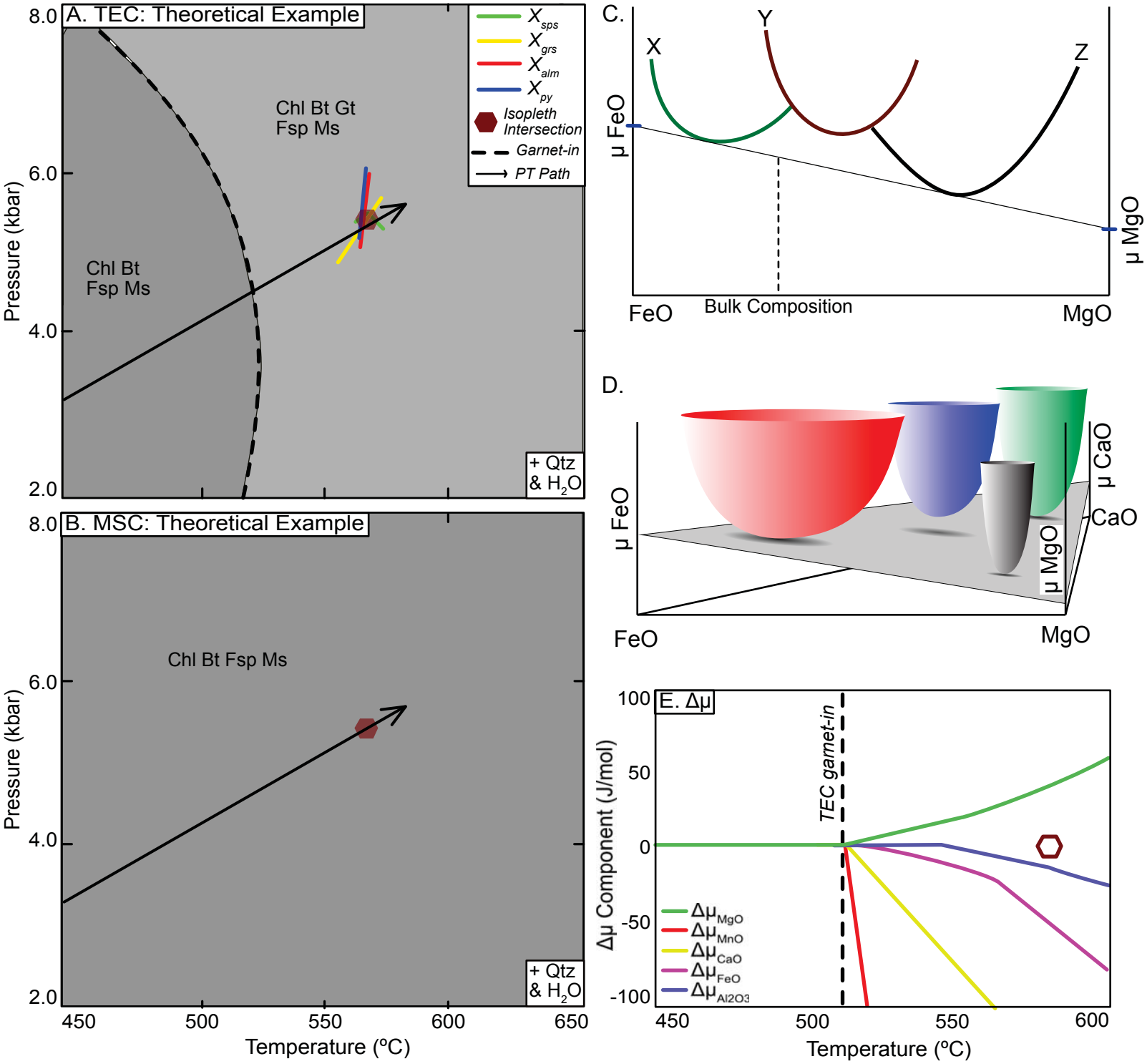
A. TEC: Theoretical Example
Chl Bt Gt
Fsp Ms
Chl Bt
Fsp Ms
+ Qtz
& H2O
Isopleth
Intersection
Garnet-in
PT Path
Pressure (kbar)
8.0
6.0
4.0
2.0
B. MSC: Theoretical Example
Chl Bt Fsp Ms
+ Qtz
& H2O
450
500
550
600
650
Temperature (ºC)
C.
X
Y
Z
μ FeO
μ MgO
FeO
Bulk Composition
MgO
D.
μ FeO
μ CaO
μ MgO
CaO
FeO
MgO
E. Δμ
TEC garnet-in
Δμ Component (J/mol)
100
50
0
-50
-100
ΔμMgO
ΔμMnO
ΔμCaO
ΔμFeO
ΔμAl2O3
450
500
550
600
Temperature (ºC)

Figure 1

Figure 2

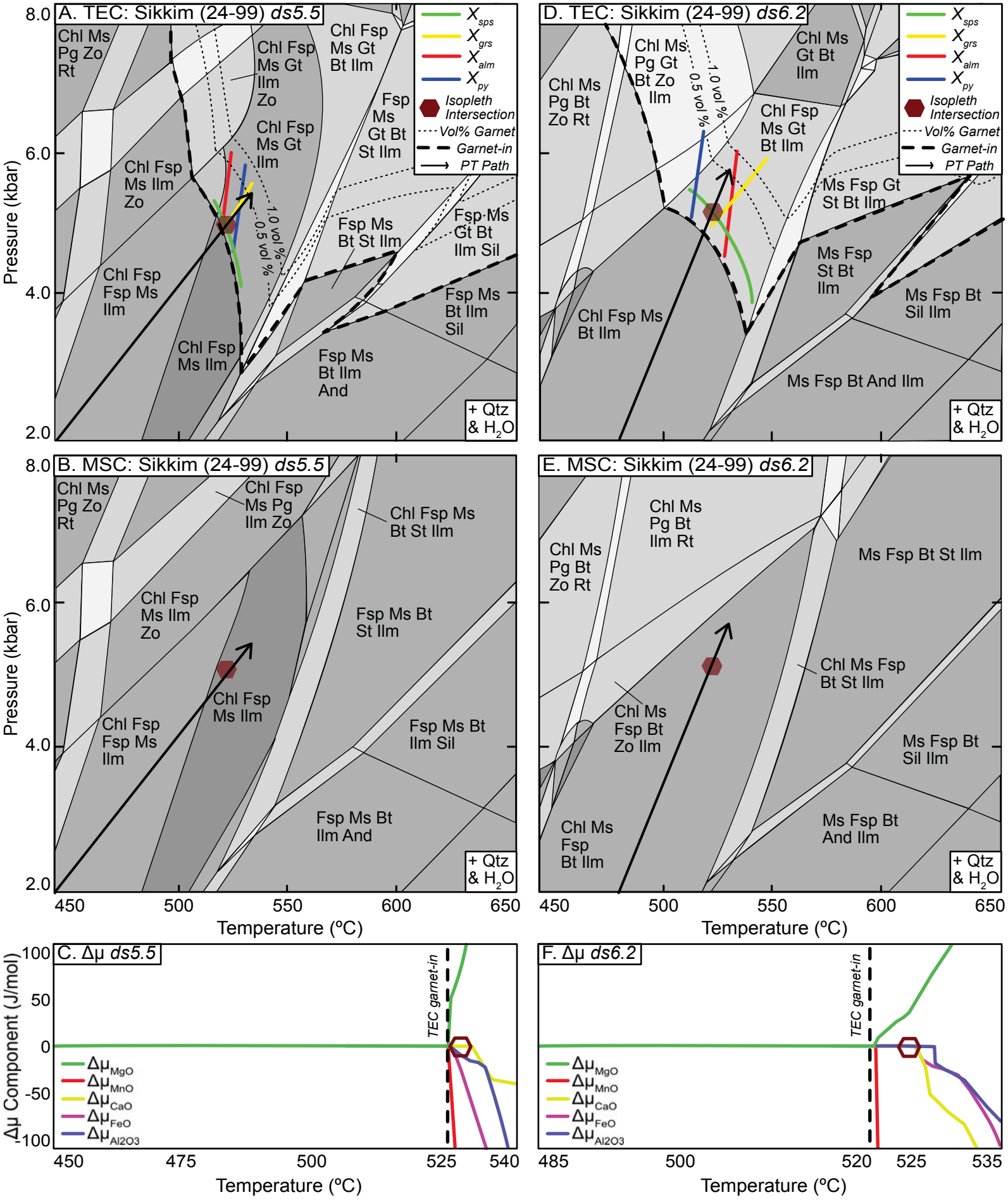
A. TEC: Sikkim (24-99) ds5.5
D. TEC: Sikkim (24-99) ds6.2
B. MSC: Sikkim (24-99) ds5.5
E. MSC: Sikkim (24-99) ds6.2
C. Δμ ds5.5
F. Δμ ds6.2
Pressure (kbar)
Temperature (°C)
Δμ Component (J/mol)
+ Qtz & H2O
Isopleth Intersection
Vol% Garnet
Garnet-in
PT Path
1.0 vol %
0.5 vol %
TEC garnet-in
Chl Ms Pg Zo Rt
Chl Fsp Ms Gt Ilm Zo
Chl Fsp Ms Gt Bt Ilm
Fsp Ms Gt Bt St Ilm
Chl Fsp Ms Ilm Zo
Fsp Ms Bt St Ilm
Fsp Ms Gt Bt Ilm Sil
Chl Fsp Fsp Ms Ilm
Fsp Ms Bt Ilm Sil
Chl Fsp Ms Ilm
Fsp Ms Bt Ilm And
Chl Ms Pg Gt Bt Zo Ilm
Chl Ms Gt Bt Ilm
Chl Ms Pg Bt Zo Rt
Ms Fsp Gt St Bt Ilm
Ms Fsp St Bt Ilm
Ms Fsp Bt Sil Ilm
Chl Fsp Ms Bt Ilm
Ms Fsp Bt And Ilm
Chl Ms Pg Zo Rt
Chl Fsp Ms Pg Ilm Zo
Chl Fsp Ms Bt St Ilm
Fsp Ms Bt St Ilm
Chl Fsp Ms Ilm Zo
Chl Fsp Ms Ilm
Chl Fsp Fsp Ms Ilm
Fsp Ms Bt Ilm Sil
Fsp Ms Bt Ilm And
Chl Ms Pg Bt Ilm Rt
Ms Fsp Bt St Ilm
Chl Ms Fsp Bt St Ilm
Chl Ms Fsp Bt Zo Ilm
Ms Fsp Bt Sil Ilm
Chl Ms Fsp Bt Ilm
Ms Fsp Bt And Ilm
Δμ MgO
Δμ MnO
Δμ CaO
Δμ FeO
Δμ Al2O3

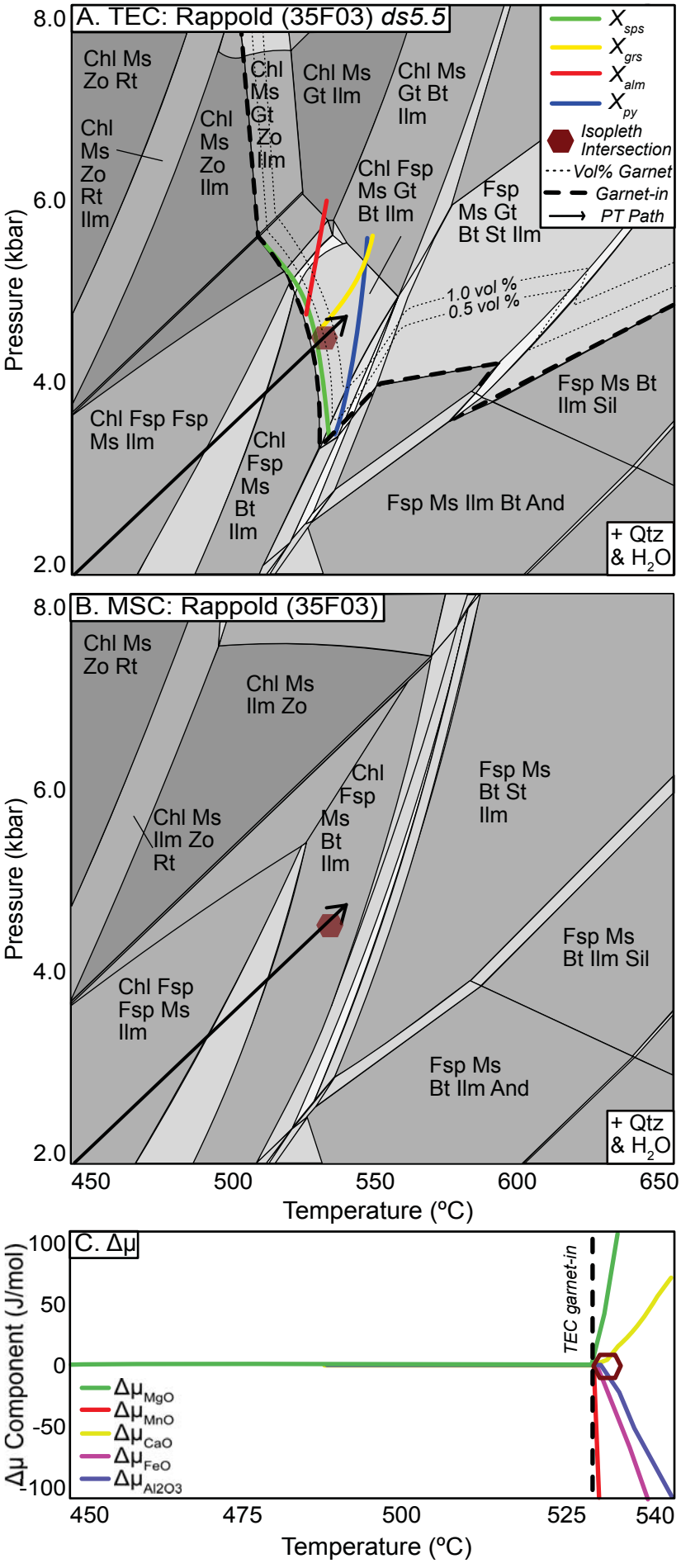
A. TEC: Rappold (35F03) ds5.5
Chl Ms Zo Rt
Chl Ms Zo Rt Ilm
Chl Ms Zo Ilm
Chl Ms Gt Zo Ilm
Chl Ms Gt Ilm
Chl Ms Gt Bt Ilm
Chl Fsp Ms Gt Bt Ilm
Fsp Ms Gt Bt St Ilm
1.0 vol %
0.5 vol %
Fsp Ms Bt Ilm Sil
Chl Fsp Fsp Ms Ilm
Chl Fsp Ms Bt Ilm
Fsp Ms Ilm Bt And
+ Qtz & H2O
Xsps
Xgrs
Xalm
Xpy
Isopleth Intersection
Vol% Garnet
Garnet-in
PT Path
Pressure (kbar)
8.0
6.0
4.0
2.0
B. MSC: Rappold (35F03)
Chl Ms Zo Rt
Chl Ms Ilm Zo
Chl Ms Ilm Zo Rt
Chl Fsp Ms Bt Ilm
Fsp Ms Bt St Ilm
Fsp Ms Bt Ilm Sil
Chl Fsp Fsp Ms Ilm
Fsp Ms Bt Ilm And
+ Qtz & H2O
Pressure (kbar)
8.0
6.0
4.0
2.0
450
500
550
600
650
Temperature (ºC)
C. Δμ
TEC garnet-in
Δμ MgO
Δμ MnO
Δμ CaO
Δμ FeO
Δμ Al2O3
Δμ Component (J/mol)
100
50
0
-50
-100
450
475
500
525
540
Temperature (ºC)

Figure 3

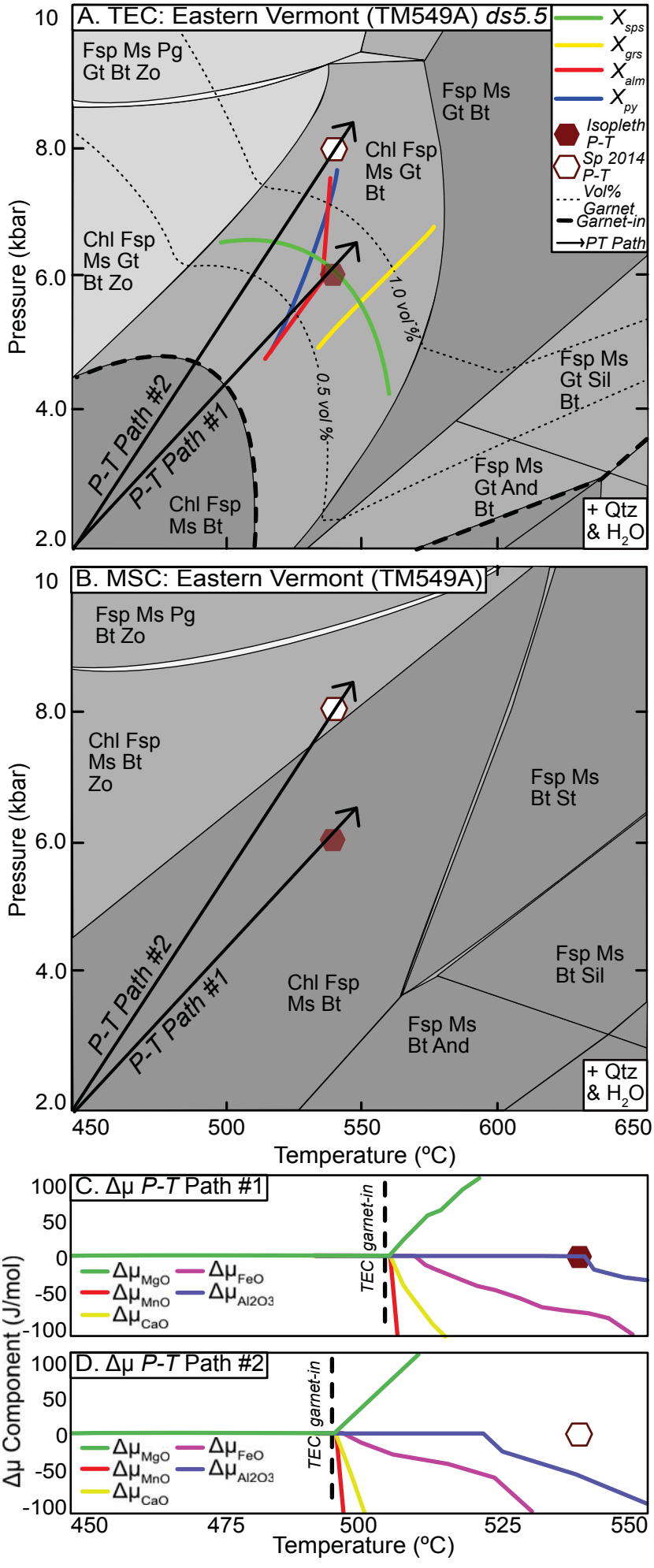
A. TEC: Eastern Vermont (TM549A) ds5.5
Fsp Ms Pg Gt Bt Zo
Fsp Ms Gt Bt
Chl Fsp Ms Gt Bt
Chl Fsp Ms Gt Bt Zo
Fsp Ms Gt Sil Bt
Fsp Ms Gt And Bt
Chl Fsp Ms Bt
+ Qtz & H2O
P-T Path #2
P-T Path #1
1.0 vol %
0.5 vol %
Xsps
Xgrs
Xalm
Xpy
Isopleth P-T
Sp 2014 P-T
Vol% Garnet
Garnet-in
PT Path
Pressure (kbar)
B. MSC: Eastern Vermont (TM549A)
Fsp Ms Pg Bt Zo
Chl Fsp Ms Bt Zo
Fsp Ms Bt St
Fsp Ms Bt Sil
Chl Fsp Ms Bt
Fsp Ms Bt And
Temperature (°C)
C. Δμ P-T Path #1
D. Δμ P-T Path #2
TEC garnet-in
ΔμMgO
ΔμFeO
ΔμMnO
ΔμAl2O3
ΔμCaO
Δμ Component (J/mol)

Figure 4

Figure 5

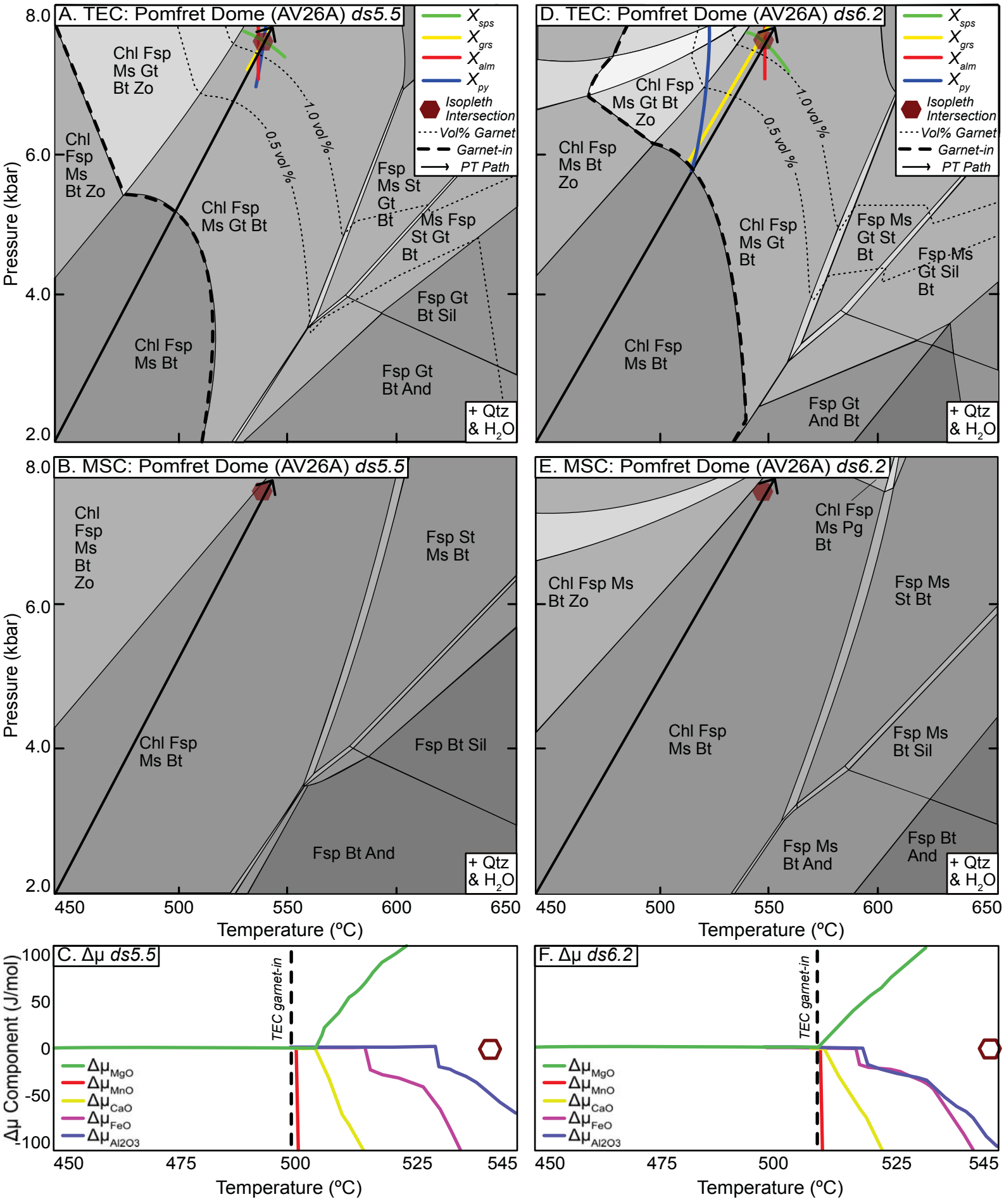
A. TEC: Pomfret Dome (AV26A) ds5.5
D. TEC: Pomfret Dome (AV26A) ds6.2
B. MSC: Pomfret Dome (AV26A) ds5.5
E. MSC: Pomfret Dome (AV26A) ds6.2
C. Δμ ds5.5
F. Δμ ds6.2
Pressure (kbar)
Temperature (ºC)
Δμ Component (J/mol)
Chl Fsp Ms Gt Bt Zo
Chl Fsp Ms Bt Zo
Chl Fsp Ms Gt Bt
Fsp Ms St Gt Bt
Ms Fsp St Gt Bt
Fsp Gt Bt Sil
Chl Fsp Ms Bt
Fsp Gt Bt And
Fsp Ms Gt St Bt
Fsp-Ms Gt Sil Bt
Fsp Gt And Bt
Chl Fsp Ms Pg Bt
Chl Fsp Ms Bt Zo
Fsp Ms St Bt
Fsp Bt Sil
Fsp Ms Bt Sil
Fsp Ms Bt And
Fsp Bt And
+ Qtz & H2O
1.0 vol %
0.5 vol %
Isopleth Intersection
Vol% Garnet
Garnet-in
PT Path
TEC garnet-in
ΔμMgO
ΔμMnO
ΔμCaO
ΔμFeO
ΔμAl2O3

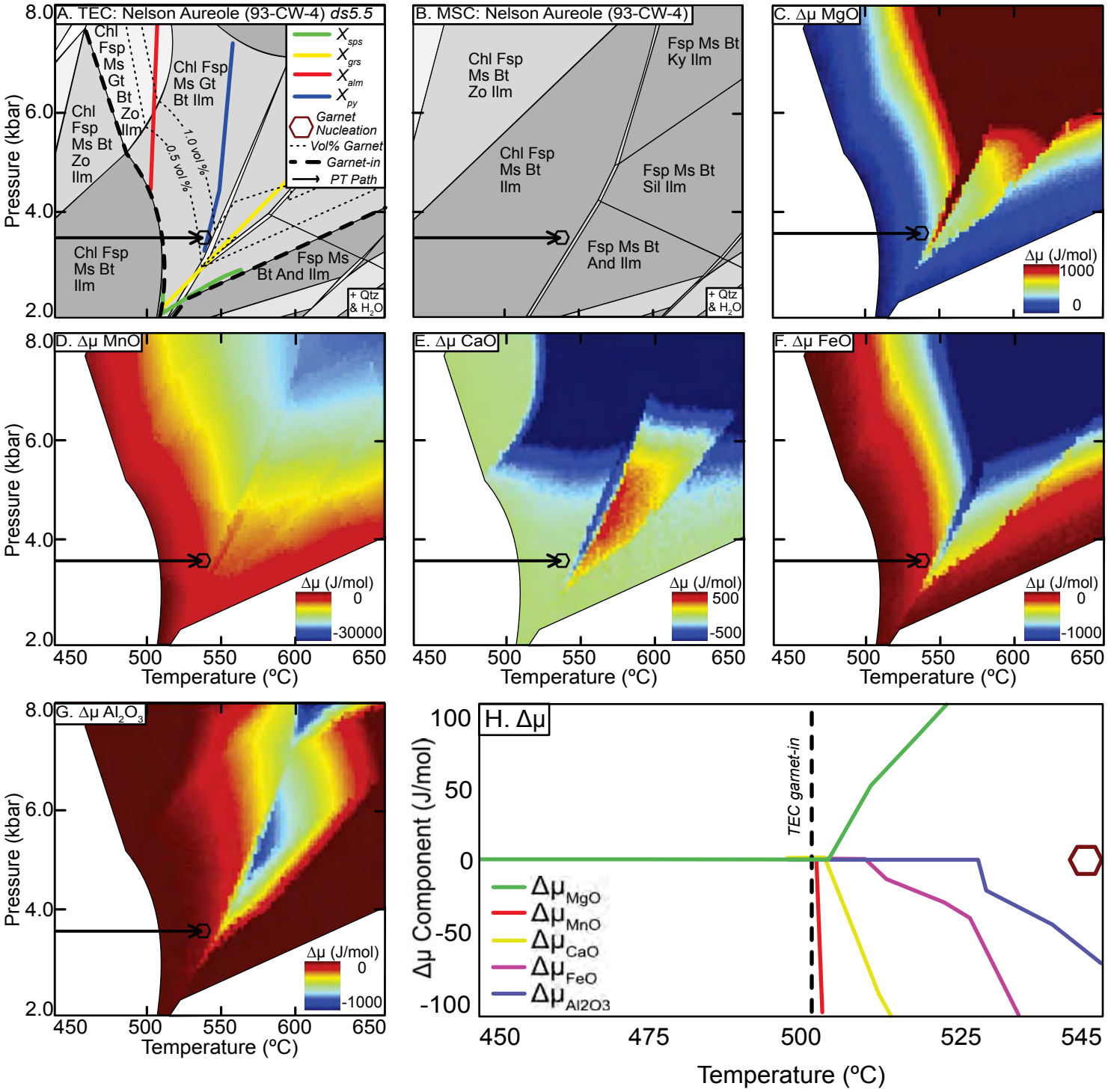
A. TEC: Nelson Aureole (93-CW-4) ds5.5
B. MSC: Nelson Aureole (93-CW-4)
C. Δμ MgO
D. Δμ MnO
E. Δμ CaO
F. Δμ FeO
G. Δμ Al2O3
H. Δμ
Pressure (kbar)
Temperature (ºC)
Δμ Component (J/mol)
TEC garnet-in
Garnet Nucleation
Vol% Garnet
Garnet-in
PT Path
+ Qtz & H2O

Figure 6

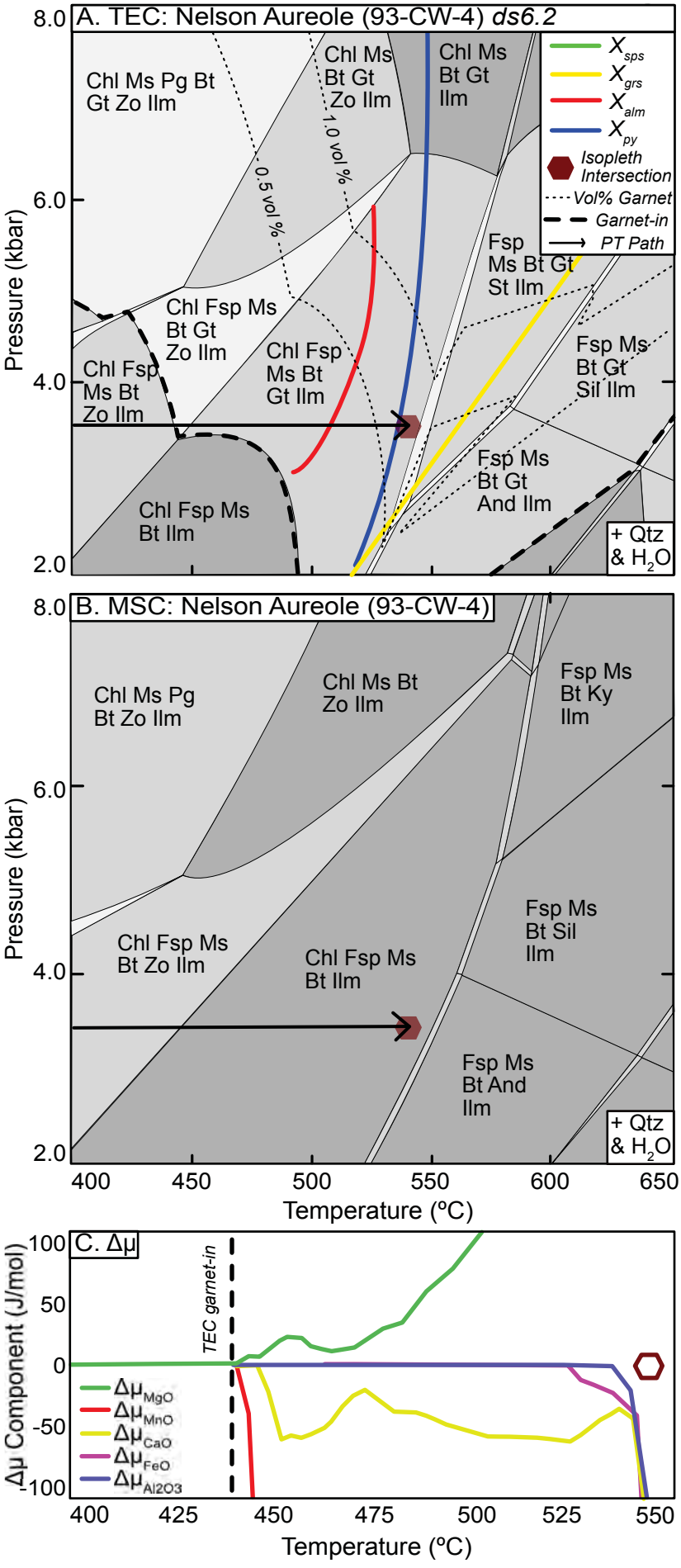
A. TEC: Nelson Aureole (93-CW-4) ds6.2
Chl Ms Pg Bt Gt Zo Ilm
Chl Ms Bt Gt Zo Ilm
Chl Ms Bt Gt Ilm
0.5 vol %
1.0 vol %
Chl Fsp Ms Bt Gt Zo Ilm
Chl Fsp Ms Bt Zo Ilm
Chl Fsp Ms Bt Gt Ilm
Fsp Ms Bt Gt St Ilm
Fsp Ms Bt Gt Sil Ilm
Fsp Ms Bt Gt And Ilm
Chl Fsp Ms Bt Ilm
+ Qtz & H2O
Xsps
Xgrs
Xalm
Xpy
Isopleth Intersection
Vol% Garnet
Garnet-in
PT Path
Pressure (kbar)
8.0
6.0
4.0
2.0
B. MSC: Nelson Aureole (93-CW-4)
Chl Ms Pg Bt Zo Ilm
Chl Ms Bt Zo Ilm
Fsp Ms Bt Ky Ilm
Chl Fsp Ms Bt Zo Ilm
Chl Fsp Ms Bt Ilm
Fsp Ms Bt Sil Ilm
Fsp Ms Bt And Ilm
+ Qtz & H2O
Pressure (kbar)
8.0
6.0
4.0
2.0
400
450
500
550
600
650
Temperature (°C)
C. Δμ
TEC garnet-in
Δμ MgO
Δμ MnO
Δμ CaO
Δμ FeO
Δμ Al2O3
Δμ Component (J/mol)
100
50
0
-50
-100
400
425
450
475
500
525
550
Temperature (°C)

Figure 7

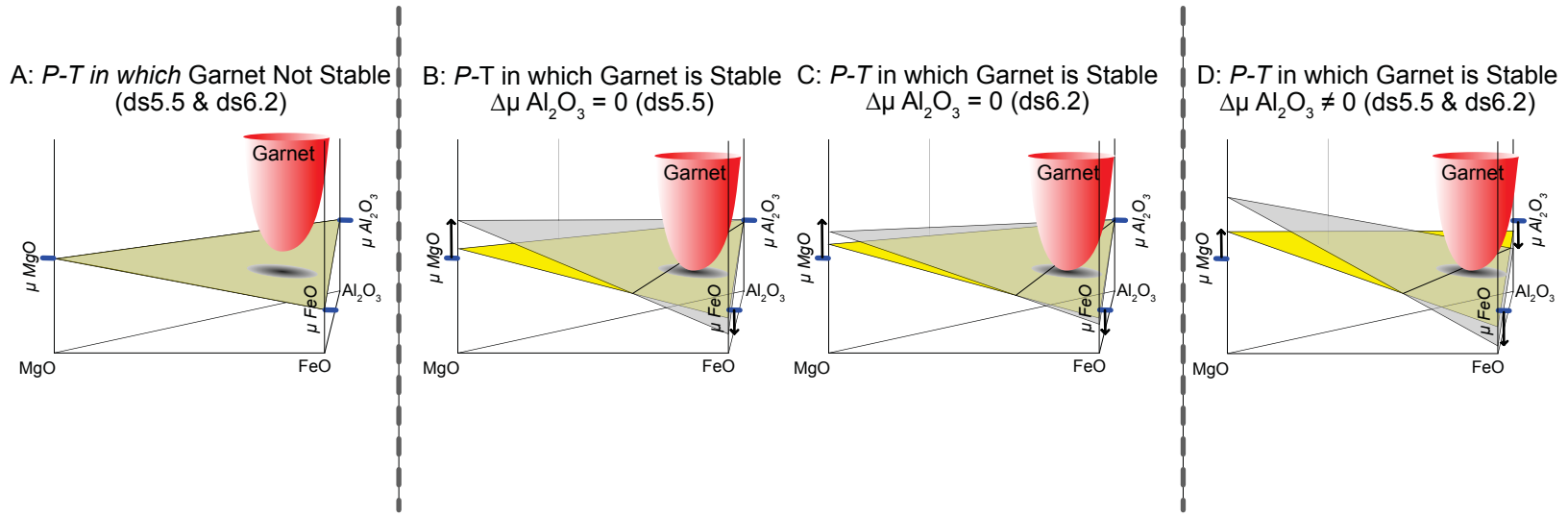
A: *P-T in which* Garnet Not Stable (ds5.5 & ds6.2)
B: *P*-T in which Garnet is Stable $\Delta\mu\ Al_2O_3 = 0$ (ds5.5)
C: *P-T* in which Garnet is Stable $\Delta\mu\ Al_2O_3 = 0$ (ds6.2)
D: *P-T* in which Garnet is Stable $\Delta\mu\ Al_2O_3 \neq 0$ (ds5.5 & ds6.2)
Garnet
μ MgO
μ $Al_2O_3$
μ FeO
$Al_2O_3$
MgO
FeO

Figure 8

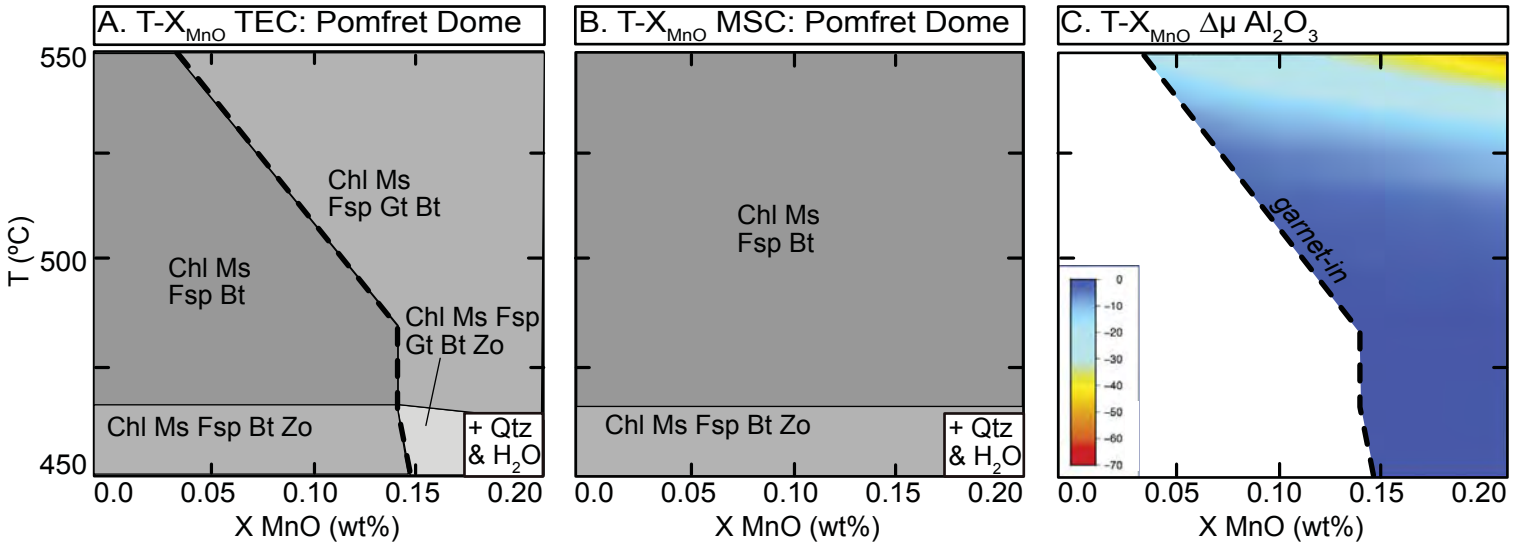
A. T-X$_{MnO}$ TEC: Pomfret Dome
B. T-X$_{MnO}$ MSC: Pomfret Dome
C. T-X$_{MnO}$ Δμ Al$_2$O$_3$
T (°C)
550
500
450
Chl Ms
Fsp Gt Bt
Chl Ms
Fsp Bt
Chl Ms Fsp
Gt Bt Zo
Chl Ms Fsp Bt Zo
+ Qtz
& H$_2$O
Chl Ms
Fsp Bt
Chl Ms Fsp Bt Zo
+ Qtz
& H$_2$O
garnet-in
0
-10
-20
-30
-40
-50
-60
-70
0.0
0.05
0.10
0.15
0.20
X MnO (wt%)

Figure 9